https://doi.org/10.5194/mr-2020-30
Preprint. Discussion started: 20 November 2020

Open Access MAGNETIC RESONANCE Discussions

Heteronuclear and Homonuclear Finite Pulse Radio Frequency Driven Recoupling

Authors: Evgeny Nimerovsky*, Kai Xue, Kumar Tekwani Movellan & Loren B. Andreas*

Affiliations:

Department of NMR based Structural Biology, Max Planck Institute for Biophysical Chemistry, Am Fassberg 11, Göttingen, Germany

*Corresponding authors: land@nmr.mpibpc.mpg.de ORCID: 0000-0003-3216-9065 and evni@nmr.mpibpc.mpg.de

Abstract

Homonuclear finite-pulse radio frequency driven recoupling (fp-RFDR) has been broadly used in multi-dimensional magic-angle spinning (MAS) solid-state NMR experiments over the past 20 years. The theoretical and the simulated descriptions of this method were presented during that time, resulting in an understanding of the influence of chemical shift offset, finite pulse effects, and dipolar truncation. Here we present an operator analysis of both heteronuclear and homonuclear fp-RFDR. By numerical simulation, we show which operators are involved in the longitudinal exchange for both heteronuclear and the well-known homonuclear sequences. This results in a better understanding of the influence of phase cycling of the fp-RFDR pulses, which is typically a variant of XY cycling. We investigate the heteronuclear and homonuclear fp-RFDR signals and evolution of the operators through the fp-RFDR block. We show the convergence of the evolutions of the heteronuclear and homonuclear fp-RFDR signals at even numbers of rotor periods and completely different evolution between them. We demonstrate heteronuclear ^{1}H- ^{13}C and ^{1}H-^{15}N fp-RFDR magnetization transfer using a microcrystalline SH3 sample at 100 kHz MAS.

https://doi.org/10.5194/mr-2020-30
Preprint. Discussion started: 20 November 2020

Keywords: Magic Angle Spinning NMR, homonuclear and heteronuclear fpRFDR, the operator analysis

Introduction

Solid-state magic-angle spinning NMR spectroscopy is used to obtain atomic resolution physical and chemical knowledge about the investigated sample. One of the abilities of the NMR experiments is to determine distance between a pair of spin 1/2 nuclei via recoupling the homonuclear(A. E. Bennett et al. 1992; Ok et al. 1992; Z. Zhang et al. 2020; Gelenter, Dregni, and Hong 2020; Takegoshi, Nakamura, and Terao 2001; Szeverenyi, Sullivan, and Maciel 1982; Hou, Yan, et al. 2011; Hou et al. 2013; Carravetta et al. 2000; Andrew E. Bennett et al. 1998) or heteronuclear(Gelenter, Dregni, and Hong 2020; T. Gullion and Schaefer 1989; Jaroniec, Filip, and Griffin 2002; Hing, Vega, and Schaefer 1992; Hartmann and Hahn 1962; Rovnyak 2008; Metz, Wu, and Smith 1994; Hediger et al. 1994; Hou, Byeon, et al. 2011; Brinkmann and Levitt 2001; Gelenter and Hong 2018; Z. Zhang, Chen, and Yang 2016) dipolar interactions. The homonuclear fp-RFDR sequence is successfully applied for the qualitative and quantitative determinations of the dipolar spin correlations in materials(Saalwächter 2013; Messinger et al. 2015; Fritz et al. 2019; Roos, Mandala, and Hong 2018; Nishiyama et al. 2014; Wong et al. 2020; Hellwagner et al. 2018; Pandey and Nishiyama 2018) and biomolecular samples(Zheng, Qiang, and Weliky 2007; Tang, Berthold, and Rienstra 2011; Shen et al. 2012; Pandey et al. 2014; Grohe et al. 2019; Andreas et al. 2015; Petkova et al. 2002; Aucoin et al. 2009; Zinke et al. 2018; R. Zhang, Mroue, and Ramamoorthy 2017; Zhou et al. 2012; Jain et al. 2017; Colvin et al. 2015; Shi et al. 2015; Daskalov et al. 2020).

These applications depend on a firm quantum mechanical foundation. One of the theoretical tools to investigate the influence of radio frequency (RF) pulse sequences on the spin system is Average Hamiltonian Theory(Haeberlen and Waugh 1968; Maricq 1982) (AHT). The two necessary conditions for application of the AHT are(Ernst, Bodenhausen, and Wokaun 1987):

1. The total Hamiltonian has to be periodic;

https://doi.org/10.5194/mr-2020-30
Preprint. Discussion started: 20 November 2020

Open Access MAGNETIC RESONANCE Discussions

2. The stroboscopic measurements are synchronized with the period, or cycle time, of the total Hamiltonian.

When these conditions are fulfilled, the time-dependent Hamiltonian, evaluated at multiples of the cycle time, can be replaced by the sum of the time-independent multiple order averaging terms(Ernst, Bodenhausen, and Wokaun 1987).

AHT simplifies quantum calculations, especially in cases when complex multiple-pulse sequences are used. It can explain the selectivity of the pulse sequence, meaning to find the experimental conditions under which the desired interactions are recoupled and undesired decoupled. However, AHT can predict the state of the spin system at specific time points only and not the paths by which the spin system is evolves during the period when rf pulses are given. Another successful method, Floquet Theory(Levante et al. 1995; Scholz, van Beek, and Ernst 2010), allows to consider the Hamiltonian at any point of time. However, such analysis is complicated with a transformation to infinity-dimensional Hilbert space(Levante et al. 1995).

Homonuclear transfer of the magnetization via longitudinal exchange occurs with a rotor-synchronized train of π-pulses, with one pulse each rotor period. The method is called radio-frequency driven recoupling(A. E. Bennett et al. 1992) (RFDR), or simple excitation for the dephasing of rotational-echo amplitudes(Terry Gullion and Vega 1992). This sequence has two different AHT descriptions of the recoupling of homonuclear dipolar interactions, depending on the experimental conditions(Ok et al. 1992; Ishii 2001).

In the first case, delta π-pulses are assumed. The efficiency to recouple homonuclear dipolar interaction is linked with the difference between isotropic chemical shifts of the dipolar linked spins, S_k and S_l (A. E. Bennett et al. 1992; Terry Gullion and Vega 1992; Andrew E. Bennett et al. 1998). The evolution of the spin system at specific time points is described with a flip-flop part of zero-quantum

https://doi.org/10.5194/mr-2020-30
Preprint. Discussion started: 20 November 2020

Open Access MAGNETIC RESONANCE Discussions

dipolar Hamiltonian: $I_k^+ I_l^- + I_k^- I_l^+$ (A. E. Bennett et al. 1992; Andrew E. Bennett et al. 1998; Nielsen et al. 1994; Ok et al. 1992; Bayro et al. 2009; Sodickson et al. 1993; Straasø et al. 2016).

For the second theoretical description, finite π-pulses are considered (fpRFDR)(A. E. Bennett et al. 1992; Ishii 2001; Nishiyama, Zhang, and Ramamoorthy 2014; R. Zhang et al. 2015; Brinkmann, Schmedt auf der Günne, and Levitt 2002; Ji et al. 2020). The efficiency of recoupling of the homonuclear dipolar interaction is directly linked with a duty factor(Ishii 2001) – the ratio between the width of π-pulse and the width of the rotor period. AHT predicts restoring of the whole zero-quantum dipolar Hamiltonian, $3I_{kz}I_{lz} - \bar{I}_k\bar{I}_l$,under fast and ultra-fast MAS rates.(Ishii 2001)

Both these theoretical descriptions consider the same experiment with the same phase cycling, traditionally XY8 (Terry Gullion, Baker, and Conradi 1990). Although the influence of the different phase cycling schemes was investigated in different articles(Ok et al. 1992; Nishiyama, Zhang, and Ramamoorthy 2014; R. Zhang et al. 2015; Ji et al. 2020), the main conclusion to the contribution from phase cycling to the transfer of the RFDR signal was a reduction of influence from resonance offsets and pulse errors(A. E. Bennett et al. 1992; Ishii 2001).

In this article we investigate both heteronuclear and homonuclear fpRFDR experiments using numerical tools to track the system at any arbitrary time. Using the simulated and the theoretical analysis we show that for fpRFDR experiments the typical phase cycling, XY(Ishii 2001; Nishiyama, Zhang, and Ramamoorthy 2014; R. Zhang et al. 2015; Hellwagner et al. 2018), plays a crucial role in the transfer of magnetization between a pair of spins. Under fast and ultra-fast MAS rates the heteronuclear and homonuclear fpRFDR experiments can be described with the same model Hamiltonian, but only at increments of the rotor period. The evolutions of the operators, however, are completely different for heteronuclear and homonuclear cases between these points. For the experimental demonstrations we perform heteronuclear 1D ^{1}H-{^{13}C} and ^{1}H-{^{15}N} fp-RFDR experiments using α-PET (Movellan et al. 2019) labeled SH3 at 100 kHz MAS.

https://doi.org/10.5194/mr-2020-30
Preprint. Discussion started: 20 November 2020

Open Access MAGNETIC RESONANCE Discussions

Theory

The fp-RFDR sequence consists of a train of π-pulses every one rotor period (Fig.1a). The length of the repeated block is defined by the phase cycling: XYn (n=4, 8, 16, 32), resulting in a time of nT_R (Ishii 2001). Measurements are, in the simplest case, restricted to occur every nT_R. In our simulations as well as in the experiments we used XY8 phase cycling.

To evaluate the operator, $\hat{A}$, between the time points t_i and $t_i + t_x$ we first have to solve the von Neumann equation ($\hbar = 1$):

$$\frac{d\rho}{dt} = -i[H(t), \rho(t)], \quad \text{Eq. (1.1)}$$

where $H(t)$ is a Hamiltonian of the spin system and $\rho(t)$ is a density matrix. The formal solution of the Eq. (1.1) (Ernst, Bodenhausen, and Wokaun 1987) is:

$$\rho(t_i + t_x) = \hat{T} exp\left\{-i \int_{t_i}^{t_i+t_x} dt\, H(t)\right\} \rho(t_i) \hat{T} exp\left\{-i \int_{t_i}^{t_i+t_x} dt\, H(t)\right\}, \text{ Eq. (1.2)}$$

where $\hat{T}$ is a Dyson Operator.

The evaluated operator, $\hat{A}(t_i + t_x)$ is:

$$\hat{A}(t_i + t_x) = Tr\{\hat{A}\rho(t_i + t_x)\} \text{ Eq. (1.3)}$$

One of the possibilities to deal with a Dyson Operator in Eq. (1.2), in order to propagate forward in time from the point t_i to $t_i + t_x$, is to split one propagator into a product of N propagators(Nimerovsky and Goldbourt 2012):

$$\hat{T} exp\left\{-i \int_{t_i}^{t_i+t_x} dt\, H(t)\right\} = \lim_{N\to\bowtie} \prod_{k=1}^{N} exp\left\{-i \int_{t_i+t_x-\Delta_{x,i}k}^{t_i+t_x-\Delta_{x,i}(k-1)} dt\, H(t)\right\}, \ \Delta_{x,i} = t_x/N \quad \text{Eq. (1.4).}$$

It allows to omit the Dyson Operator and perform the simulations correctly. This is the way that calculations are performed in the popular SIMPSON software(Bak, Rasmussen, and Nielsen 2000). The main difference in our implementation of numerical evolutions with respect to SIMSPON calculations is

https://doi.org/10.5194/mr-2020-30
Preprint. Discussion started: 20 November 2020

to use analytical integrations rather than numerical integrations, which significantly reduces the computer time.

Each of the rotor periods of the fp-RFDR sequence can be divided into two parts with the lengths of t_p (defined with the length of π-pulse and $T_R - t_p$ (the delay, Fig. 1a). The numerical calculations split each of these two parts into N subparts with the lengths t_p/N and $(T_R - t_p)/N$, respectively. Fig. 1b shows the transferred fp-RFDR signals for I_3 spin system under different values of N. Solid lines represent the transferred $I_2 \rightarrow I_3$ signal between a weakly coupled dipolar pair with 66 Hz dipolar interaction, whereas the dotted lines represent the $I_2 \rightarrow I_2$ signal. With an increase in the value of N, the simulated signals converge and under N=16 (red lines) and N=32 (black lines) the signals coincide. It means that under N≥16, the simulations provide the correct evolution of the spin system. In all numerical calculations we used N=32.

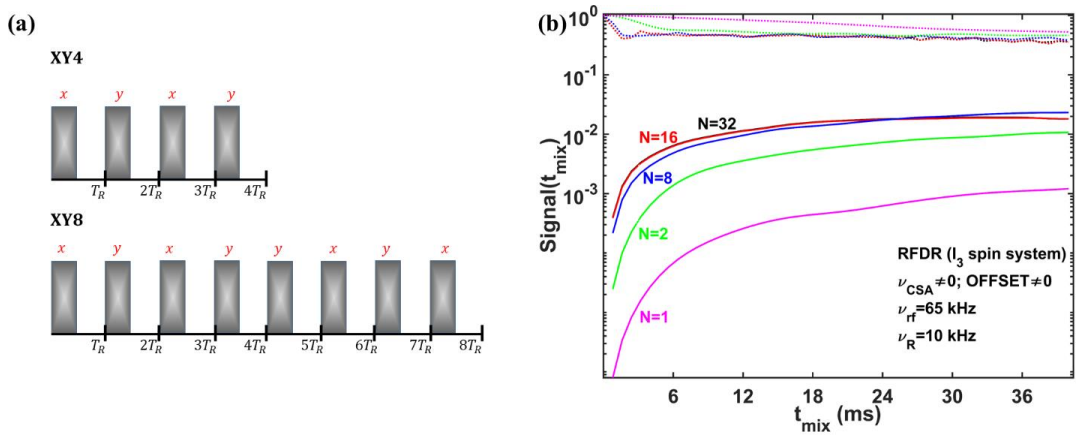

Fig. 1 (a) Finite Pulse RFDR block consisting of four π-pulses every rotor period with phase cycling: *x, y, x, y* (XY4) or eight π-pulses with phase cycling: *x, y, x, y, y, x, y, x* (XY8). (b) Simulated I_3 spin system under 10 kHz of MAS and 65 kHz of rf-field, dipolar values of $\nu_{12} = 66$ Hz, $\nu_{13} = 150$ Hz, $\nu_{23} = 2.15$ kHz, and offset values of $\Omega_1 = -8$ kHz, $\Omega_2 = 9$ kHz, $\Omega_3 = -7$ kHz and CSA values of $\nu_{CSA,1} = 9.2$ Hz, f $\nu_{CSA,2} = 2.5$ Hz, f $\nu_{CSA,3} = 8$ kHz. Axis Y shows the intensities of the starting and transferred signals between different operators, $I_{z2} \rightarrow I_{z2}$ (the dotted lines) and $I_{z2} \rightarrow I_{z1}$ (the solid lines), under different values of N: 1 (magenta lines), 2 (green lines), 8 (blue lines), 16 (red lines) and 32 (black lines). The values of the dipolar interactions and MAS rate were taken from Ref. [(Bayro et al. 2009)]. XY8 phase cycling was used.

https://doi.org/10.5194/mr-2020-30
Preprint. Discussion started: 20 November 2020

Open Access MAGNETIC RESONANCE Discussions

Figs. A1-2 show the transferred fp-RFDR signals for I_3 and IS_2 spin systems under different simulated conditions and validation by comparison with SIMSPON simulations of fp-RFDR signals.

In the next 'Simulations' section we firstly consider the evolution of the I_3 spin system under the RFDR sequence. We investigate the influence of each part of the Dipolar Hamiltonian (the secular and the flip-flop parts) on the measured operators at specific time points under different simulated conditions.

In the subsequent subsections we compare the behavior of I_2 and IS spin systems under RFDR. We consider the evolutions of all operators and their amplitude at different time points. We demonstrate with simulations and provide the theoretical analysis (applying the fictitious spin ½ operator formalism(Vega 1978)) of the influence of the phase cycling on the transfer of fp-RFDR signal. We shows the paths with which the signals are transferred between different spins for heteronuclear and homonuclear spin systems.

Simulations

The full high field truncated dipolar Hamiltonian of I_3 spin system is represented as follows:

$H_{D,Full} = 0.5\sum \omega_{D,rs}(t)[3I_{zr}I_{zs} - I_rI_s] = 0.5\sum \omega_{D,rs}(t)[3I_{zr}I_{zs} - I_{zr}I_{zs} - 0.5(I_r^+I_s^- + I_r^-I_s^+)]$, Eq. (2.1)

where $\omega_{D,rs}(t)$ is a periodic dipolar time dependent function(Olejniczak, Vega, and Griffin 1984) between spins I_r and I_s. This Hamiltonian is subsequently referred, to as the full Hamiltonian, and contains only the A and B terms of the dipolar alphabet(Slichter 1990).

Firstly we investigate which part of the full high field dipolar Hamiltonian can be a model Hamiltonian. A model Hamiltonian is a simplified Hamiltonian, which provides the same evolution of the spin system at specific time points as a full dipolar Hamiltonian. We consider 3 model Hamiltonians:

$H_D = 1.5\sum \omega_{D,rs}(t)I_{zr}I_{zs}$, Eq. (2.2a) $\qquad H_D = -0.5\sum \omega_{D,rs}(t)I_rI_s$, Eq. (2.2b)

$$H_D = -0.25\sum \omega_{D,rs}(t)[I_r^+I_s^- + I_r^-I_s^+] \text{ .} \quad \text{Eq. (2.2c)}$$

https://doi.org/10.5194/mr-2020-30
Preprint. Discussion started: 20 November 2020

Open Access MAGNETIC RESONANCE Discussions

Eq. (2.2a) contains a secular part of the dipolar Hamiltonian (Eq. (2.1)), whereas the scalar products, $I_r I_S$, are omitted. Eq. (2.2b) contains the scalar products of the dipolar Hamiltonian only. Eq. (2.2c) contains the flip-flop parts of the Dipolar Hamiltonian. The Figs. 2-4 show the evolution of a I_3 spin system under these three model Hamiltonians (Eq. (2.2a) – red lines; Eq. (2.2b) – green lines; Eq. (2.2c) – pink lines) and comparison with the full Dipolar Hamiltonian (Eq. 2.1 – black lines).

Fig. 2 shows the transferred signals under 10 kHz of MAS, when only dipolar interactions are taken into account. Under these conditions the secular dipolar Hamiltonian (Fig. 2a, red lines) provides similar values of the amplitudes of the operators at specific time points (the simulated measurement occurred every $8T_R$, with XY8 phase cycling, as with the full Dipolar Hamiltonian (Fig. 2a, black lines). The scalar product dipolar Hamiltonian (Fig. 2b, green lines) and the flip-flop dipolar Hamiltonian (Fig. 2b, pink lines) provide different results with respect to the full Dipolar Hamiltonian (Fig. 2b, black lines).

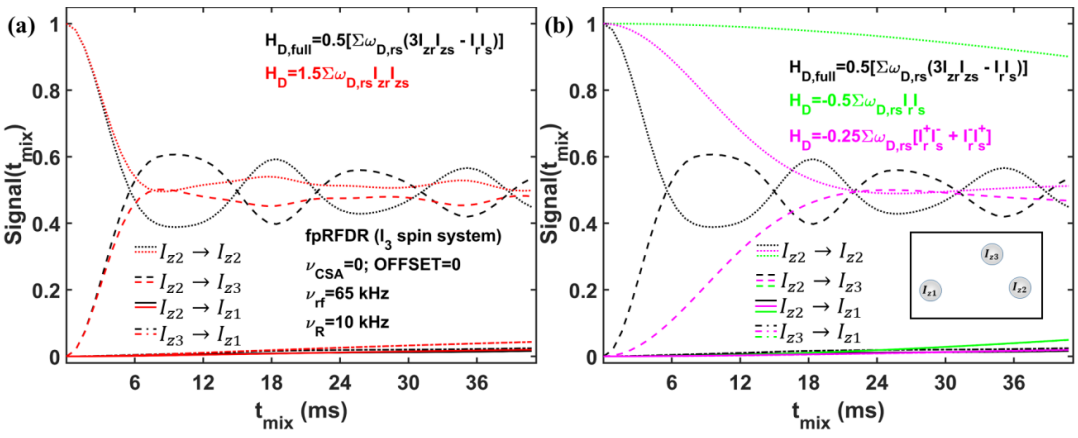

Fig. 2 Simulated I_3 spin system under 10 kHz of MAS and 65 kHz of rf-field, dipolar coupling values of $\nu_{12} = 66$ Hz, $\nu_{13} = 150$ Hz, $\nu_{23} = 2.15$ kHz (the schematic spin arrangement is shown in the insert of (b)) and zero values of offset and CSA. Axis Y shows the intensities of the starting and transferred signals between different operators: $I_{z2} \rightarrow I_{z2}$ (the dotted lines); $I_{z2} \rightarrow I_{z3}$ (the dashed lines); $I_{z2} \rightarrow I_{z1}$ (the solid lines); $I_{z3} \rightarrow I_{z1}$ (the dashed-dotted lines). (a) The black lines represent the signals, simulating with the full dipolar Hamiltonian (Eq. 2.1). The red lines represent the signals, simulating with the secular model Hamiltonian (Eq. 2.2a). (b) The black lines represent the signals, simulating with the full dipolar Hamiltonian (Eq. 2.1). The green lines represent the signals, simulating with the scalar product model Hamiltonian (Eq. 2.2b). The magenta lines represent the signals,

https://doi.org/10.5194/mr-2020-30
Preprint. Discussion started: 20 November 2020

Open Access MAGNETIC RESONANCE Discussions

simulating with the scalar product model Hamiltonian (Eq. 2.2c). The values of the dipolar interactions and MAS rate was taken from Ref. [(Bayro et al. 2009)]. XY8 phase cycling was used.

The conclusions are reversed when we add chemical shift offsets that have similar values with respect to the MAS frequency (Fig. 3). In the simulations CSA values were also added into simulations. However, the main influence comes from the offset as shown in Fig. (A2). The secular dipolar Hamiltonian (Fig. 3a, red lines) provides completely different results with respect to the full dipolar Hamiltonian (Fig. 3a, black lines), whereas the scalar product dipolar Hamiltonian (Fig. 3b, green lines) and the flip-flop dipolar Hamiltonian (Fig. 3b, pink lines) provide similar results as the full dipolar Hamiltonian (Fig. 3b, black lines).

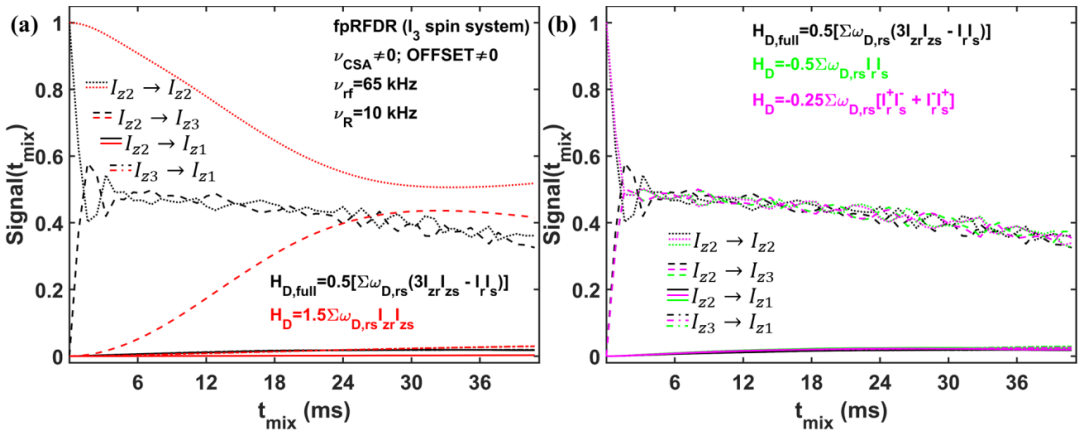

Fig. 3 Simulated I_3 spin system under 10 kHz of MAS and 65 kHz of rf-field, dipolar coupling values of $\nu_{12} = 66$ Hz, $\nu_{13} = 150$ Hz, $\nu_{23} = 2.15$ kHz, offset values of $\Omega_1 = -8$ kHz, $\Omega_2 = 9$ kHz, $\Omega_3 = -7$ kHz, and CSA values of $\nu_{CSA,1} = 9.2$ Hz, f $\nu_{CSA,2} = 2.5$ Hz, f $\nu_{CSA,3} = 8$ kHz. Axis Y shows the intensities of the starting and transferred signals between different operators: $I_{z2} \rightarrow I_{z2}$ (the dotted lines); $I_{z2} \rightarrow I_{z3}$ (the dashed lines); $I_{z2} \rightarrow I_{z1}$ (the solid lines); $I_{z3} \rightarrow I_{z1}$ (the dashed-dotted lines). (a) The black lines represent the signals, simulating with the full dipolar Hamiltonian (Eq. 2.1). The red lines represent the signals, simulating with the secular model Hamiltonian (Eq. 2.2a). (b) The black lines represent the signals, simulating with the full dipolar Hamiltonian (Eq. 2.1). The green lines represent the signals, simulating with the scalar product model Hamiltonian (Eq. 2.2b). The magenta lines represent the signals, simulating with the scalar product model Hamiltonian (Eq. 2.2c). The values of the dipolar interactions and MAS rate were taken from Ref. [(Bayro et al. 2009)]. XY8 phase cycling was used.

https://doi.org/10.5194/mr-2020-30
Preprint. Discussion started: 20 November 2020

Open Access MAGNETIC RESONANCE Discussions

When the spinning frequency is increased such that it is significantly larger than the offsets, the situation again reverses. Fig. 4 shows the evolution of the spin system under 90 kHz MAS with the same offset and CSA values as in Fig. 3. Under such conditions the secular dipolar Hamiltonian (Fig. 4a, red lines) provides similar results as a full dipolar Hamiltonian (Fig. 3a, black lines), whereas the scalar product dipolar Hamiltonian (Fig. 4b, green lines) and the flip-flop dipolar Hamiltonian (Fig. 4b, pink lines) provide different results with respect to full dipolar Hamiltonian (Fig. 4b, black lines).

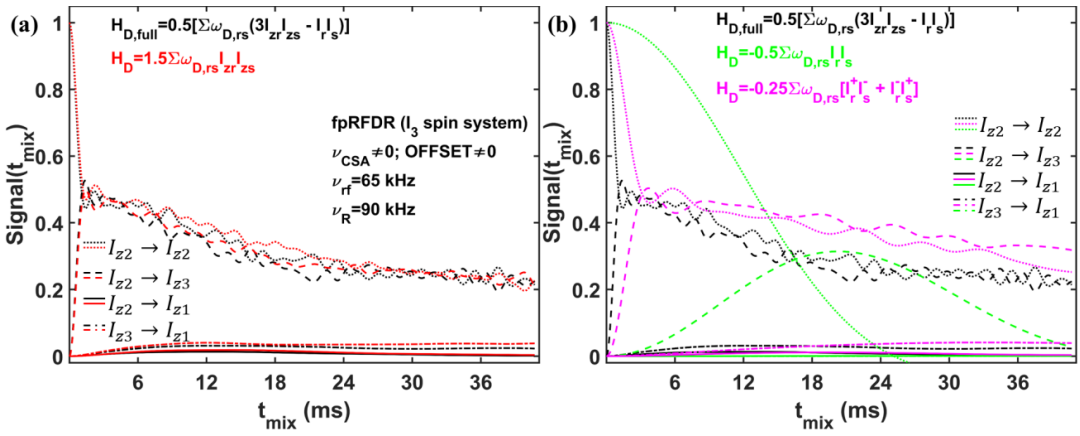

Fig. 4 Simulated I_3 spin system under 90 kHz of MAS and 65 kHz of rf-field, dipolar coupling values of $\nu_{12} = 66$ Hz, $\nu_{13} = 150$ Hz, $\nu_{23} = 2.15$ kHz, offset values of $\Omega_1 = -8$ kHz, $\Omega_2 = 9$ kHz, $\Omega_3 = -7$ kHz, and CSA values of $\nu_{CSA,1} = 9.2$ Hz, f $\nu_{CSA,2} = 2.5$ Hz, f $\nu_{CSA,3} = 8$ kHz. Axis Y shows the intensities of the starting and transferred signals between different operators: $I_{z2} \rightarrow I_{z2}$ (the dotted lines); $I_{z2} \rightarrow I_{z3}$ (the dashed lines); $I_{z2} \rightarrow I_{z1}$ (the solid lines); $I_{z3} \rightarrow I_{z1}$ (the dashed-dotted lines). (a) The black lines represent the signals, simulating with the full dipolar Hamiltonian (Eq. 2.1). The red lines represent the signals, simulating with the secular model Hamiltonian (Eq. 2.2a). (b) The black lines represent the signals, simulating with the full dipolar Hamiltonian (Eq. 2.1). The green lines represent the signals, simulating with the scalar product model Hamiltonian (Eq. 2.2b). The magenta lines represent the signals, simulating with the scalar product model Hamiltonian (Eq. 2.2c). The values of the dipolar interactions and MAS rate were taken from Ref. [(Bayro et al. 2009)]. XY8 phase cycling was used.

Considering these three cases, we can conclude that for fp-RFDR, when the difference of the offset values between spins are significantly smaller with respect to the used MAS rate, the simplified secular Hamiltonian (Eq. 2.1a) can play a significant role in the transfer. Such a simplified model

https://doi.org/10.5194/mr-2020-30
Preprint. Discussion started: 20 November 2020

Open Access MAGNETIC RESONANCE Discussions

Hamiltonian correctly describes the evolution of the spin systems at specific time points. In the case when offset values are comparable with the MAS rate, the flip-flop Hamiltonian (Eq. 2.1c) can play a role of the simplified model Hamiltonian. The second conclusion coincides with the theoretical analysis previously obtained with AHT for that sequence(A. E. Bennett et al. 1992; Andrew E. Bennett et al. 1998; Nielsen et al. 1994; Ok et al. 1992; Bayro et al. 2009; Sodickson et al. 1993; Straasø et al. 2016), whereas the first conclusion diverges – dependence on the zero-quantum dipolar operator(Ishii 2001) for AHT. The second conclusion allows the transfer of the magnetization between homonuclear spins only, whereas the first conclusion supposes that a heteronuclear fp-RFDR transfer is also possible.

For the heteronuclear spin system, the full high field dipolar Hamiltonian is secular. The main difference to the heteronuclear full dipolar Hamiltonian with a homonuclear model Hamiltonian (Eq. 2.1a) is a factor of 1.5. On the basis of the first conclusion, for fully heteronuclear spin systems all dipolar interactions should be 1.5 times larger with respect to the homonuclear dipolar values to obtain the same signals as for a fully homonuclear spin system. For a more comprehensive investigation of the behaviors of the homonuclear and heteronuclear spin systems under fpRFDR, we consider below I_2 and *IS* spin systems.

The simulations allow us to consider the evolutions within a Cartesian operator basis set of the two spin system(Ernst, Bodenhausen, and Wokaun 1987). For the two spin system, the basis set consists of 16 operators. The evolution of each of them is described by microscopic amplitude:

$$a_k(t_{mix}) = Tr\{\hat{K}\rho(t_{mix})\}, \quad \text{Eq. (2.3)}$$

where $\hat{K}$ is an operator of the spin system. The macroscopic amplitude is represented as follow:

$$A_k = \int d\Omega\, a_k(t_{mix}), \qquad \text{Eq. (2.4)}$$

where the integration is performed over all Euler angles. Summing all amplitudes in squares, the next condition should be performed:

https://doi.org/10.5194/mr-2020-30
Preprint. Discussion started: 20 November 2020

$$\sum |a_k|^2 (t_{mix}) = 1 \quad \text{Eq. (2.5)}$$

Fig. 5 shows the macroscopic amplitudes (Eq. 2.4) of 14 operators under different offset values for *IS* (a, c, e, g) and I_2 (b, d, f, h) spin systems. In all Figs. the initial operator is I_z for the heteronuclear case and I_{z1} for the homonuclear spin systems and the MAS rate is 10 kHz. The pink dashed lines represent the sum of the square amplitudes (Eq. (2.5)).

For the on-resonance condition (Fig. 5a) the evolution of the *IS* spin system is described with four operators only: I_z (black line), S_z (green line), $2I_xS_y$ (blue line) and $2I_yS_x$ (red line). The pink dashed line shows the sum of the squares of amplitudes of these four operators. The other 11 operators are not excited and have zero amplitudes. For an I_2 spin system (Fig. 5b) the evolution is identical as for an *IS* spin system, when the measurements are taken every two rotor periods.

With a 3 kHz offset difference between the spins (Fig. 5c), we find the excitation of all 14 operators. However, only six of them have significant amplitudes. Additionally to the previously mentioned four operators, we see significant amplitudes for $2I_xS_x$ (cyan line) and $2I_yS_y$ (purple line) operators. Compared to the on-resonance case, the velocity of the transfer of the signal from I_z to S_z operators (green line) decreased for the *IS* spin system (Fig. 5c). For the I_2 spin system (Fig. 5d) the velocity of the transfer of the signal from I_{z1} to I_{z2} operators (green line) as well as the velocities of the evolutions of other operators significantly increased.

For a 5 kHz offset difference and heteronuclear *IS* spins (Fig. 5e), we do not see any transfer of the signal from I_z operator to S_z operator, whereas for the I_2 spin system (Fig. 5f), the velocities of the excitation of all operators increased more as compared to the previous cases. Also for this case only the 6 previously mentioned operators have significant macroscopic amplitudes.

Under a 9 kHz offset difference and heteronuclear *IS* spins (Fig. 5g), we see again the transfer of the signal from I_z operator to S_z operator (Fig. 5g, green line). Also more operators have significant macroscopic amplitudes. For the I_2 spin system (Fig. 5h), the transfer of signal from I_{z1} to I_{z2} operators

https://doi.org/10.5194/mr-2020-30
Preprint. Discussion started: 20 November 2020

Open Access MAGNETIC RESONANCE Discussions

(green line) has the largest velocity with respect to previous cases. Also here we see more transfer of the signal from I_{z1} to other operators, however with smaller amplitudes in comparison with the *IS* case.

For negligible offset differences with respect to the MAS rate, the evolution of the operators of *IS* and I_2 spin systems are the same at specific time points. However, when offsets are comparable with the MAS rate, we obtain completely different evolution for these systems. With increase of offset difference the *IS* spin system passes through specific rotor resonance condition (the difference between offsets equal to half of the MAS rate), under which the transfer does not occur. For the I_2 spin system the velocity of the transfer increases with increased offset difference.

https://doi.org/10.5194/mr-2020-30
Preprint. Discussion started: 20 November 2020

Open Access MAGNETIC RESONANCE Discussions

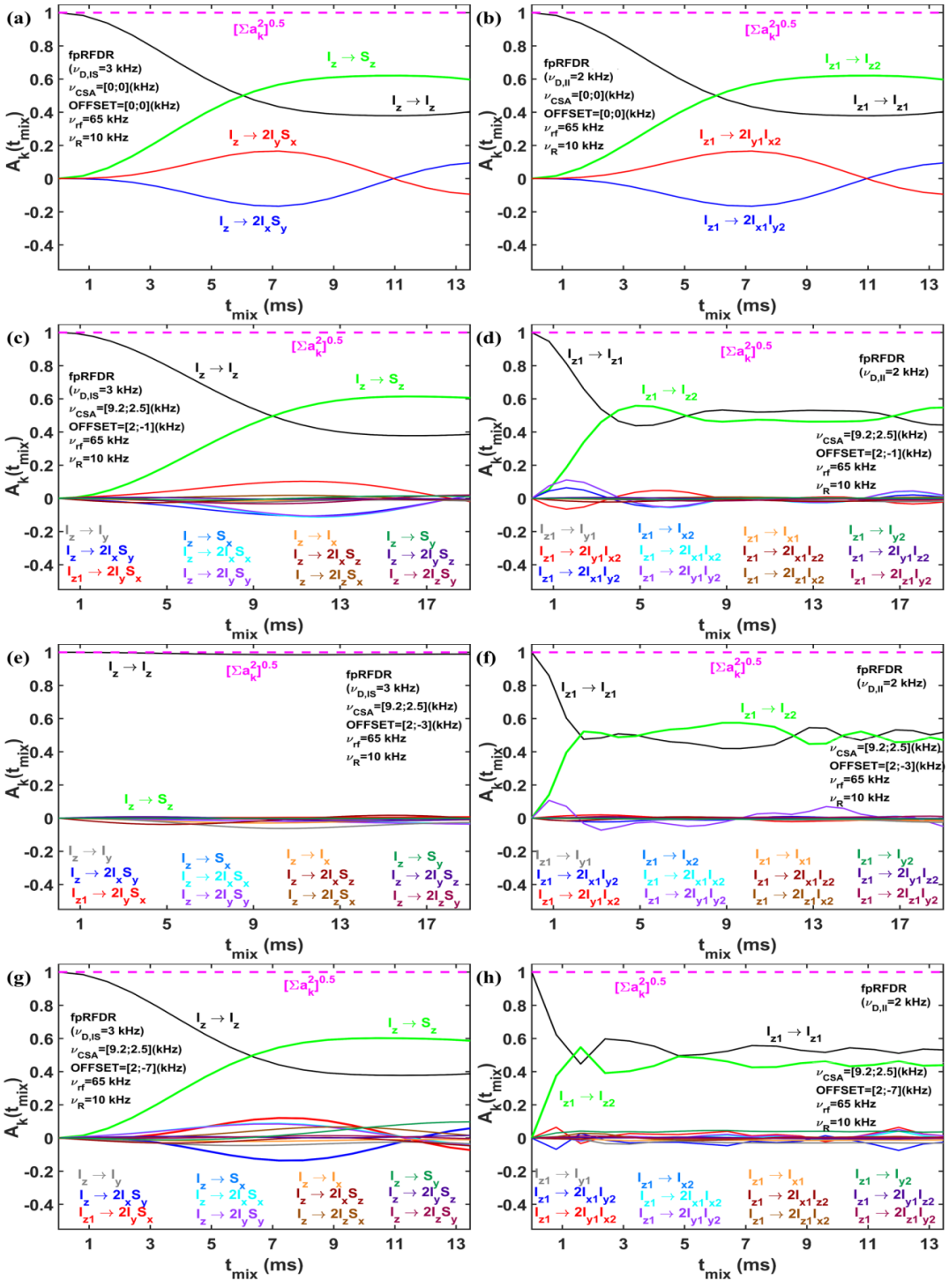

269

https://doi.org/10.5194/mr-2020-30
Preprint. Discussion started: 20 November 2020

Open Access MAGNETIC RESONANCE Discussions

Fig. 5 The simulated amplitudes of the operators for *IS* ((a), (c), (e), (g) – $\nu_{D,IS} = 3$ kHz, the initial operator is I_z) and I_2 ((b), (d), (f), (h) – $\nu_{D,II} = 2$ kHz, the initial operator is I_{z1}) spin systems under 10 kHz of MAS rate and 65 kHz of rf-field. The pink dashed line represent the sum of the squared amplitudes (Eq. (2.5)), which are shown in the Figs. Black lines – I_z and I_{z1}; Green lines – S_z and I_{z2}; Blue lines – $2I_xS_y$ and $2I_{x1}I_{y2}$; Red lines – $2I_yS_x$ and $2I_{y1}I_{x2}$; Cyan lines – $2I_xS_x$ and $2I_{x1}I_{x2}$; Purple lines – $2I_yS_y$ and $2I_{y1}I_{y2}$; Azure lines –S_x and I_{x2}; Dark green lines – S_y and I_{y1}; Orange lines – I_x and I_{x1}; Grey lines – I_y and I_{y1}; Crimson red lines – $2I_xS_z$ and $2I_{x1}I_{z2}$; Brown lines – $2I_zS_x$ and $2I_{z1}I_{x2}$; Jazzberry Jam lines – $2I_zS_y$ and $2I_{z1}I_{y2}$; Indigo lines – $2I_yS_z$ and $2I_{y1}I_{z2}$. (a) and (b) – Offset values in kHz: 0, 0; CSA values in kHz: 0, 0. (c) and (d) – Offset values in kHz: 2, -1; CSA values in kHz: 9.2, 2.5. (e) and (f) – Offset values in kHz: 2, -3; CSA values in kHz: 9.2, 2.5. (g) and (h) – Offset values in kHz: 2, -7; CSA values in kHz: 9.2, 2.5.

Figs. 5a and b showed the indentical evolutions of the same operators for *IS* and *I*2 spin system at specific time points (every two rotor periods). A more interesting case is a comparison of the evolution of these operators between specific time points, between 0 and $2T_R$. Fig. 6 shows the microscopic amplitudes (Eq. 2.4) of the operators during first two rotor periods. The time scale of that two rotor periods can be devided into four parts: $t(\pi_x) \rightarrow del_1 \rightarrow t(\pi_y) \rightarrow del_2$. For increasing the effect of the transfer we simulated with 15 kHz and 10 kHz for the dipolar interactions for *IS* and I_2 spin systems, respectively.

Regardless the offset values, the evolutions of the operators between specific time points are completely different for *IS* (Fig. 6a and c) and I_2 spin systems (Fig. 6b and d). For the on-resonance condition, by the end of the first π_x-pulse only one operator is created for the *IS* spin system: $2I_xS_y$ (Fig. 6a, blue line). During the first delay, del_1, there is no evolution of the spin system since $[I_z, I_zS_z] = [I_xS_y, I_zS_z] = 0$. At the end of the second π_y-pulse two additional operators have nonzero amplitude: $2I_yS_x$ (Fig. 6a, red line) and S_z (Fig. 6a, green line). During the second delay, del_2, the amplitudes of these operators are not changed.

Under on-resonance conditions for the I_2 spin system (Fig. 6b) all these four operators have nonzero amplitudes in the end of the first π_x-pulse. The evolution of the I_2 spin system during this two rotor periods is much more complicated as compared to the *IS* spin system: the amplitudes of these four operators are changed during the delay times as well. However, at the end of two rotor periods the

https://doi.org/10.5194/mr-2020-30
Preprint. Discussion started: 20 November 2020

Open Access MAGNETIC RESONANCE Discussions

amplitudes of similar operators of *IS* and I_2 spin systems – I_z and I_{z1}; S_z and I_{z2}; $2I_xS_y$ and $2I_{x1}I_{y2}$; $2I_yS_x$ and $2I_{y1}I_{x2}$ – have the same values.

For a 9 kHz offset difference, in the end of the first π_x-pulse also only one operator is created for an *IS* spin system: $2I_xS_y$ (Fig. 6c, blue line). However, during the first delay, del_1, three operators are created: $2I_yS_x$ (Fig. 6c, red line), $2I_xS_x$ (Fig. 6c, cyan line) and $2I_yS_y$ (Fig. 6c, purple line). In the end of the second π_y-pulse, the operator S_z (Fig. 6c, green line) has nonzero value. However it has a very small value in comparison with the on resonance case (Fig. 6a).

For a 9 kHz offset difference, the evolution of the I_2 spin system is also described with six operators (Fig. 6d). However, in that case the I_{z2} operator has much larger amplitude in the end of two rotor periods as compared with the on resonce condition (Fig. 6b).

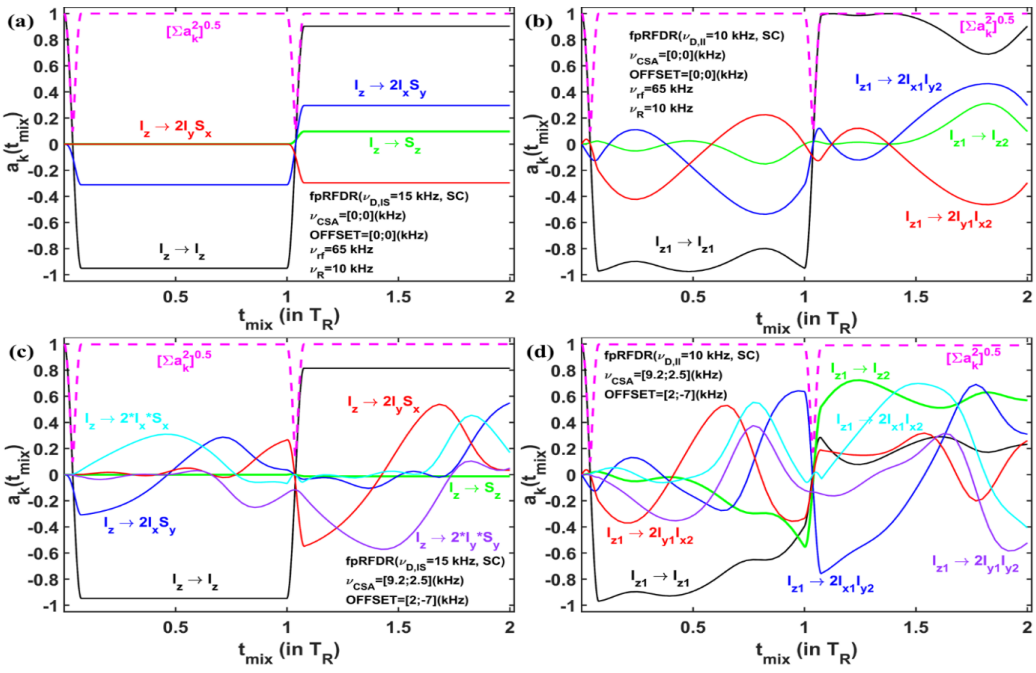

Fig. 6 The simulated amplitudes of the operators of a single crystal (Euler angles: 184°; 141°; 349°) during first rotor periods for *IS* ((a), (c) – $\nu_{D,IS}$ = 15 kHz, the initial operator is I_z) and I_2 ((b), (d) – $\nu_{D,II}$ = 10 kHz, the initial operator is I_{z1}) spin systems under 10 kHz of MAS and 65 kHz of rf-field. The pink dashed line represents the sum of the squared amplitudes (Eq. (2.5)),

https://doi.org/10.5194/mr-2020-30
Preprint. Discussion started: 20 November 2020

which are shown in Figs. Black lines – I_z and I_{z1}; Green lines – S_z and I_{z2}; Blue lines – $2I_xS_y$ and $2I_{x1}I_{y2}$; Red lines – $2I_yS_x$ and $2I_{y1}I_{x2}$; Cyan lines – $2I_xS_x$ and $2I_{x1}I_{x2}$; Purple lines – $2I_yS_y$ and $2I_{y1}I_{y2}$. (a) and (b) – Offset values in kHz: 0, 0; CSA values in kHz: 0, 0. (c) and (d) – Offset values in kHz: 2, -7; CSA values in kHz: 9.2, 2.5. The XY phase cycling was used.

Figs. 6a and b (heteronuclear and homonuclear, respectively) show completely different behavior for the amplitudes of four operators – I_z, S_z, $2I_xS_y$, $2I_yS_x$ for *IS* and I_{z1}, I_{z2}, $2I_{x1}I_{y2}$, $2I_{y1}I_{x2}$ for I_2 spin systems – during two rotor periods. However, by the end of two rotor periods, the values are the same again. For an I_2 spin system the signal is transferred to the I_{z2} operator gradually during two rotor periods (Fig. 6b green line). For *IS* spin system the signal from I_z to S_z is transferred during the second π_y-pulse only. Therefore, the phase of the second π-pulse is also the object for investigation. We considered the behavior of the amplitudes of the operators during two rotor periods when both these pulses had the same phase – $t(\pi_x) \rightarrow del_1 \rightarrow t(\pi_x) \rightarrow del_2$. Fig. 7 shows the amplitudes of the operators for *IS* (Fig. 7a) and I_2 (Fig. 7b) spin sytems. For an *IS* spin system (Fig. 7a) only two operators have nonzero amplitudes during the investigated time: I_z (black line) and $2I_xS_y$ (blue line), whereas S_z and $2I_yS_x$ are not created. For the I_2 spin system (Fig. 7b) we still detect the evalutions of all four operators. However, in the end of two rotor periods only two operators have nonzero amplitudes, as for the *IS* spin system. For both cases, there is no transfer of signal from I_z to S_z (*IS* spin system) and from I_{z1} to I_{z2} (I_2 spin system), when XX phase cycling is used. Definitelly, the phase cycling of fp-RFDR sequence plays a crucial role in the transfer of the signal between different spins.

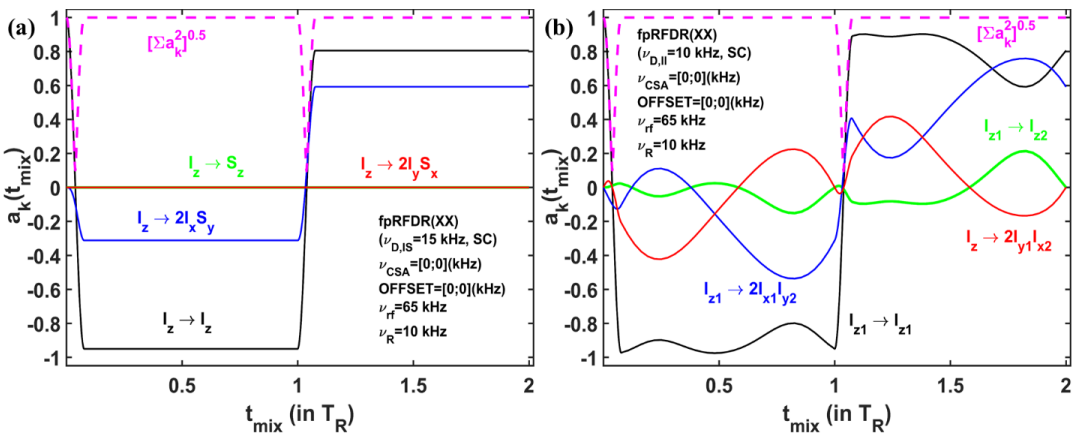

https://doi.org/10.5194/mr-2020-30
Preprint. Discussion started: 20 November 2020

Open Access MAGNETIC RESONANCE Discussions

Fig. 7 The simulated amplitudes of the operators of a single crystal (the used Euler angles: 184°; 141°; 349°) during first rotor periods for *IS* ((a) – $\nu_{D,IS}$ = 15 kHz, the initial operator is I_z) and I_2 ((b) – $\nu_{D,II}$ = 10 kHz, the initial operator is I_{z1}) spin systems under 10 kHz of MAS and 65 kHz of rf-field. The XX phase cycling was used. The pink dashed line represents the sum of the squared amplitudes (Eq. (2.5)), which are shown in Figs. Black lines – I_z and I_{z1}; Green lines – S_z and I_{z2}; Blue lines – $2I_xS_y$ and $2I_{x1}I_{y2}$; Red lines – $2I_yS_x$ and $2I_{y1}I_{x2}$; Cyan lines – $2I_xS_x$ and $2I_{x1}I_{x2}$; Purple lines – $2I_yS_y$ and $2I_{y1}I_{y2}$. Offset values in kHz: 0, 0; CSA values in kHz: 0, 0.

To understand the evolution of the *IS* operators under different phase cyclings, we can consider their evolutions during the second π-pulse only (Fig. 8). Fig. 8a shows the amplitudes during a π-pulse with y phase. During this pulse two additional operators are created. The signal is transferred from operator $2I_xS_y$ to S_z (Fig. 8a, green line) and from I_z to I_yS_x (Fig. 8b, red dashed line). During the first pulse with phase x, $2I_xS_y$ is created, whereas during the second pulse with 90° phase shifting the signal is transferred from that operator to S_z. It means that if we consider the evolution of the operators during a third π-pulse with the phase x, the transfer of the signal from I_z to operator S_z will be via the operator $2I_yS_x$. When the second π-pulse has the same phase as a first (XX), operators $2I_xS_y$ and S_z are not created and the transfer of the signal from I_z to S_z does not occur. In Appendix B we show the formal proof of zero transfer signal from I_{z1} to I_{z2} at specific time points (every one rotor period) when XX phase cycling is used.

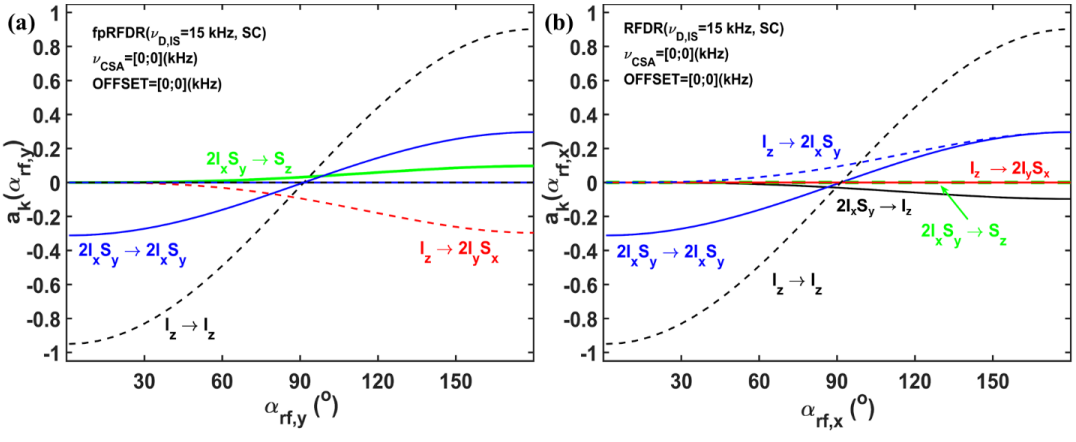

https://doi.org/10.5194/mr-2020-30
Preprint. Discussion started: 20 November 2020

Open Access MAGNETIC RESONANCE Discussions

Fig. 8 Simulated amplitudes of the operators of an IS spin system ($\nu_{D,IS}$ = 15 kHz) for a single crystal (Euler angles: 184°; 141°; 349°) during the second π-pulse with phase y (a) and x (b) under 10 kHz of MAS and with a 65 kHz rf-field. The signal is shown as a function on the pulse flip angle α. The transfer of the signal between: $2I_xS_y \rightarrow S_z$ – green solid lines; $2I_xS_y \rightarrow I_z$ – black solid lines; $I_z \rightarrow I_z$ – black dashed lines; $2I_xS_y \rightarrow 2I_xS_y$ – blue solid lines; $I_z \rightarrow 2I_xS_y$ – blue dashed lines; $I_z \rightarrow 2I_yS_x$ – red dashed lines. Offset values in kHz: 0, 0; CSA values in kHz: 0, 0.

On the basis of Fig. 6b and d, we conclude that transfer of the signal from I_{z1} to I_{z2} is more complicated than from I_z to S_z, although the same results are obtained in the end of two rotor periods. To define via which operators the homonuclear signal is transferred from one spin to another, we consider the amplitude of some operator that is generated as a result of another operator and evolution through pulses or dealys, $t(\pi_x)$, $del_1, t(\pi_y)$, and del_2 For simplicity, we first consider the *IS* spin system. Table 1 consists of four subsections, divided with different colors. The first (black color), second (green color), third (blue color) and fourth (red color) subsections represent the amplitudes of four operators, I_z, S_z, $2I_xS_y$, $2I_yS_x$, measured at four points when the initial operators are I_z, S_z, $2I_xS_y$, $2I_yS_x$, respectively.

Table 1 The microscopic amplitudes (Euler angles: 184°; 141°; 349°) of the operators (marked with bold font, the first column) in the end of four time points: π_x – in the end of first pulse; del_1 – in the end of first delay; π_y – in the end of second pulse; del_2 – in the end of second delay. The black, green, blue and red subsections represent the amplitudes with the initial operators I_z, S_z, $2I_xS_y$, $2I_yS_x$, respectively. The used simulated parameters were as in Fig. 7a.

Op	I_z				S_z				$2I_xS_y$				$2I_yS_x$			
	π_x	del_1	π_y	del_2	π_x	del_1	π_y	del_2	π_x	del_1	π_y	del_2	π_x	del_1	π_y	del_2
I_z	**-0.95**	**1**	**-0.95**	**1**	0	0	0	0	0.31	0	0	0	0	0	-0.31	0
S_z	0	0	0	0	-0.95	1	-0.95	1	0	0	-0.31	0	0.31	0	0	0
$2I_xS_y$	-0.31	0	0	0	0.31	0	0.31	0	-0.95	1	-0.95	1	0	0	0	0
$2I_yS_x$	0	0	0.31	0	0	0	0	0	0	0	0	0	-0.95	1	-0.95	1

For example, the path $I_z \xrightarrow{\pi_x} I_z \xrightarrow{del_1} I_z \xrightarrow{\pi_y} I_z \xrightarrow{del_2} I_z$ gives the amplitude of $-0.95 \cdot 1 \cdot (-0.95) \cdot 1 = 0.9$ (the bold font in the Table 1), which equals to the amplitude of the I_z operator at the end of $2T_R$ in Fig. 6a (black line). The path $I_z \xrightarrow{\pi_x} I_z \xrightarrow{del_1} I_z \xrightarrow{\pi_y} I_z \xrightarrow{del_2} S_z$ gives the amplitude of $-0.95 \cdot 1 \cdot (-0.95) \cdot 0 = 0$.

https://doi.org/10.5194/mr-2020-30
Preprint. Discussion started: 20 November 2020

Open Access MAGNETIC RESONANCE Discussions

If we analyze all possible 64 paths, we will find only one path, conecting I_z and S_z operators: $I_z \xrightarrow{\pi_x} 2I_xS_y \xrightarrow{del_1} 2I_xS_y \xrightarrow{\pi_y} S_z \xrightarrow{del_2} S_z$ with nonzero amplitude of $-0.31 \cdot 1 \cdot (-0.31) \cdot 1 = 0.097$.

In the same way we create the table for the I_2 spin system (Table 2).

Table 2 The microscopic amplitudes (Euler angles: 184°; 141°; 349°) of the operators (marked with bold font, the first column) in the end of four time points: π_x – in the end of first pulse; del_1 – in the end of first delay; π_y – in the end of second pulse; del_2 – in the end of second delay. The black, green, blue and red subsections represent the amplitudes with the initial operators I_{z1}, I_{z2}, $2I_{x1}I_{y2}$, $2I_{y1}I_{x2}$, respectively. The simulated parameters were as in Fig. 7a.

Op	I_{z1}				I_{z2}				$2I_{x1}I_{y2}$				$2I_{y1}I_{x2}$			
	π_x	del_1	π_y	del_2	π_x	del_1	π_y	del_2	π_x	del_1	π_y	del_2	π_x	del_1	π_y	del_2
$\boldsymbol{I_{z1}}$	-0.97	0.96	-0.97	0.96	0.02	0.04	0.02	0.04	0.1	-0.2	-0.21	-0.2	0.21	0.2	-0.1	0.2
$\boldsymbol{I_{z2}}$	0.02	0.04	0.02	0.04	-0.97	0.96	-0.97	0.96	0.21	0.2	-0.1	0.2	0.1	-0.2	-0.21	-0.2
$\boldsymbol{2I_{x1}I_{y2}}$	-0.1	0.21	0.21	0.2	-0.21	-0.2	0.1	-0.2	-0.97	0.96	-0.97	0.96	0.02	0.04	0.02	0.04
$\boldsymbol{2I_{y1}I_{x2}}$	-0.21	-0.2	0.1	-0.2	-0.1	0.2	0.21	0.2	0.02	0.04	0.02	0.04	-0.97	0.96	-0.97	0.96

Unlike *IS* spin system, there are 64 paths with nonzero amplitudes via which the signal is transferred from operator I_{z1} to operator I_{z2} during the first two rotor periods. 64 paths can be divided into four groups.

The first group contains eight paths with combinations of I_{z1}, I_{z2} operators only. For example, the path $I_{z1} \xrightarrow{\pi_x} I_{z1} \xrightarrow{del_1} I_{z1} \xrightarrow{\pi_y} I_{z1} \xrightarrow{del_2} I_{z2}$ has 0.0393 amplitude, whereas the path $I_{z1} \xrightarrow{\pi_x} I_{z2} \xrightarrow{del_1} I_{z2} \xrightarrow{\pi_y} I_{z2} \xrightarrow{del_2} I_{z2}$ has -0.0195 amplitude. The total amplitude of this group is 0.03920388.

The second group contains 24 paths where each of the paths contains one of the operators $2I_{x1}I_{y2}$ or $2I_{y1}I_{x2}$. For example, the path $I_{z1} \xrightarrow{\pi_x} I_{z1} \xrightarrow{del_1} I_{z1} \xrightarrow{\pi_y} 2I_{x1}I_{y2} \xrightarrow{del_2} I_{z2}$ has -0.0393 amplitude, whereas the path $I_{z1} \xrightarrow{\pi_x} I_{z1} \xrightarrow{del_1} 2I_{x1}I_{y2} \xrightarrow{\pi_y} I_{z2} \xrightarrow{del_2} I_{z2}$ has 0.0195 amplitude. The total amplitude of this group is -0.0574702.

https://doi.org/10.5194/mr-2020-30
Preprint. Discussion started: 20 November 2020

The third group contains 24 paths where each of the paths contains two of the operators $2I_{x1}I_{y2}$ or $2I_{y1}I_{x2}$. For example, the path $I_{z1} \xrightarrow{\pi_x} 2I_{y1}I_{x2} \xrightarrow{del_1} 2I_{y1}I_{x2} \xrightarrow{\pi_y} I_{z2} \xrightarrow{del_2} I_{z2}$ has 0.0393 amplitude, whereas the path $I_{z1} \xrightarrow{\pi_x} 2I_{y1}I_{x2} \xrightarrow{del_1} I_{z2} \xrightarrow{\pi_y} 2I_{y1}I_{x2} \xrightarrow{del_2} I_{z2}$ has -0.000179 amplitude. The total amplitude of this group is 0.13445302.

The fourth group contains eight paths where each of the paths contains three instances of the operators $2I_{x1}I_{y2}$, $2I_{y1}I_{x2}$. For example, the path $I_{z1} \xrightarrow{\pi_x} 2I_{y1}I_{x2} \xrightarrow{del_1} 2I_{y1}I_{x2} \xrightarrow{\pi_y} 2I_{y1}I_{x2} \xrightarrow{del_2} I_{z2}$ has -0.0393 amplitude, whereas the path $I_{z1} \xrightarrow{\pi_x} 2I_{x1}I_{y2} \xrightarrow{del_1} 2I_{x1}I_{y2} \xrightarrow{\pi_y} 2I_{x1}I_{y2} \xrightarrow{del_2} I_{z2}$ has 0.0197 amplitude. The total amplitude of this group is -0.0191567.

The total amplitude of all four groups at the time point $2T_R$ is 0.097, which is the same as for *IS* spin system.

Considering the paths of the I_2 spin system during $2T_R$ of time, we found a number of paths where the signal was transferred directly from I_{z1} to I_{z2} operators and not via $I_{x1}I_{y2}$ and $I_{y1}I_{x2}$ operators. However, it showed the microscopic amplitude at one time point only. We can calculate the powder amplitude of these paths, A_{ZZ}, as a function of the mixing time and compare with the total transferred signal from I_{z1} to I_{z2}. For simplicity of the calculations, we take into account the paths where the jump from the operator I_{z1} to I_{z2} occurs only once:

$$I_{z1} \xrightarrow{\pi_x} \dots I_{z1} \xrightarrow{t_k} I_{z2} \xrightarrow{t_{k+1}} \dots \xrightarrow{t_N} I_{z2},$$

or the paths which contain three jumps between these two operators:

$$I_{z1} \xrightarrow{\pi_x} \dots I_{z1} \xrightarrow{t_k} I_{z2} \xrightarrow{t_{k+1}} \dots I_{z2} \xrightarrow{t_{k+l}} I_{z1} \xrightarrow{t_{k+l+1}} \dots \xrightarrow{t_{k+m}} I_{z2} \xrightarrow{t_{k+m+1}} \dots \xrightarrow{t_N} I_{z2}.$$

In Fig. 9 we compare the total transferred signal (solid lines) with the direct transferred signal (dashed lines).

https://doi.org/10.5194/mr-2020-30
Preprint. Discussion started: 20 November 2020

Under on resonance condition (Fig. 9, blue lines), the contribution of the direct transferred signal to the total is very small (A_{zz}, blue dashed line) and reaches ~2% of the starting signal. Addition of offset values (red lines) increases the contribution of this transfer (red dashed line) to the total signal (red solid line), where it reaches ~16% of the starting signal. However, as can be seen the major transfer of the signal from I_{z1} to I_{z2} occurs via $I_{x1}I_{y2}$ and $I_{y1}I_{x2}$ operators for both cases.

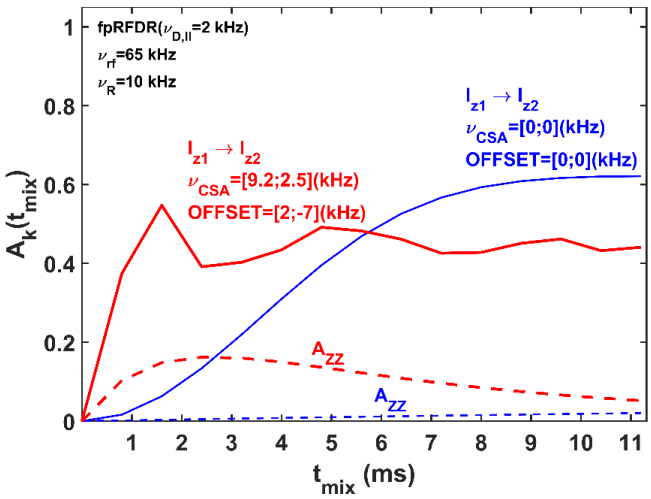

Fig. 9 The simulated total (solid lines) and the direct (dashed lines) transferred signals from operator I_{z1} to I_{z2} as a function of the mixing time. $\nu_{D,IS}$ = 15 kHz, 10 kHz of MAS and 65 kHz of rf-field. Blue lines: Offset values in kHz: 0, 0; CSA values in kHz: 0, 0. Red lines: Offset values in kHz: 2, -7; CSA values in kHz: 9.2, 2.5. The XY8 phase cycling was used.

Experiments

Fig. 10 shows a 1D heteronuclear fp-RFDR sequence. The sequence consists of two $\pi/2$-pulses on the ^{1}H channel, fp-RFDR block, $\pi/2$-pulse on the ^{13}C/^{15}N channel and detection with proton decoupling.

https://doi.org/10.5194/mr-2020-30
Preprint. Discussion started: 20 November 2020

Open Access MAGNETIC RESONANCE Discussions

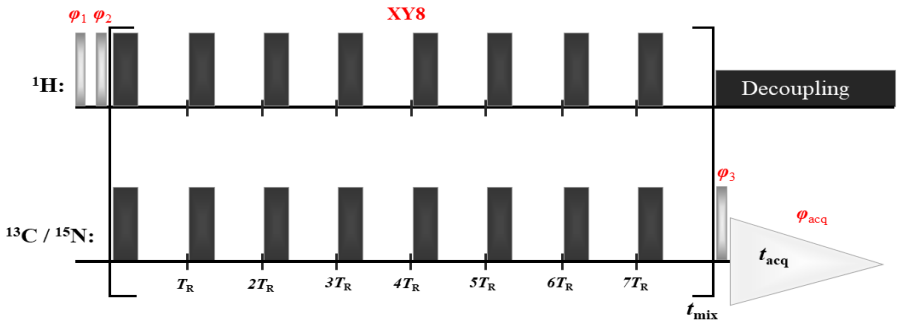

Fig. 10 1D fp-RFDR pulse sequence. The sequence consists of two π/2-pulses on the ^{1}H channel, fp-RFDR block (a train of π-pulses every one rotor period on both channels), π/2-pulse on the ^{13}C/^{15}N channel and detection with proton decoupling. The phases of the π/2-pulses are $\varphi_1 = x$; $\varphi_2 = -x, x$; $\varphi_3 = x,\ x, -x, -x$. $\varphi_{acq} = x, -x, -x,\ x$. π-pulses on the both channels followthe XY8 scheme(Terry Gullion, Baker, and Conradi 1990). During acquisition, SW$_f$-TPPM decoupling is applied on the proton channel to narrow the detected resonances(Thakur, Kurur, and Madhu 2006).

Figs. 11, 12, 13 show 1D ^{1}H-{^{13}C} fpRFDR spectra recorded with different values of the mixing time (thick blue lines), when the carbon refference frequency was set to 172 ppm, 120 ppm and 40 ppm, respectively. Red lines represent ^{1}H-{^{13}C} cross polarization (CP) spectrum at 0.8 ms of mixing time.

When the carbon reference frequency is set to 172 ppm (Fig. 11), the proton magnetization is mostly transferred to the carbonyl/carboxyl and alkene/aromatic groups. Under such conditions, the carbonyl/carboxyl signal is increased with increasing mixing time, whereas the fp-RFDR signals of the other groups are decreased. The cyan spectrum in Fig. 12c represents the control experiment – π-pulses were not applied on the ^{1}H channel during fp-RFDR and therefore zero transferred signal was measured.

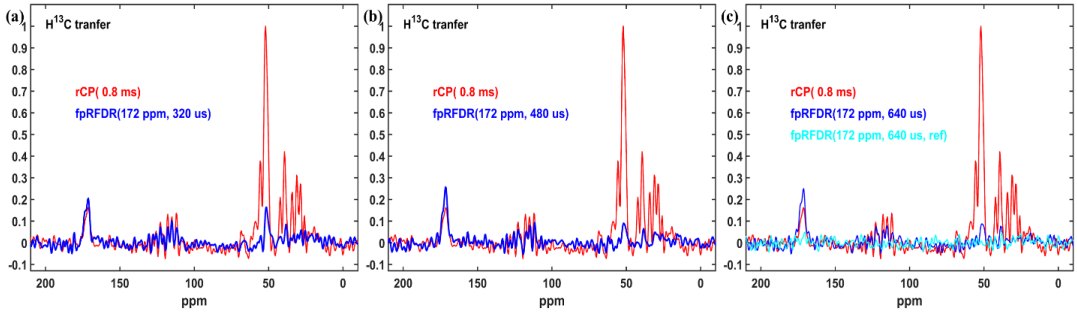

https://doi.org/10.5194/mr-2020-30
Preprint. Discussion started: 20 November 2020

Open Access MAGNETIC RESONANCE Discussions

Fig. 11 1D 1D ^{1}H-{^{13}C} ramped CP (rCP) spectrum (red line, 0.8 ms of the mixing time) and fp-RFDR spectra under different values of the mixing time: 320 us (a), 480 us (b) and 640 us (c). The cyan spectrum in (c) represents fp-RFDR experiment, when π-pulses were not applied on the ^{1}H channel. The Carbon refference frequency was set up on 172 ppm. 100 kHz MAS was used. The experimental parameters are shown in Table 3.

When the carbon refference frequency is set to 120 ppm (Fig. 12), the proton magnetization is also mostly transferred to the carbonyl/carboxyl and alkene/aromatic groups. At 320 us of transfer time, we observe an asymetry in the excitation of the alkene/aromatic carbons – the fpRFDR peaks between 120 and 110 ppm have smaller intensities compared to CP excitation, whereas the fp-RFDR peaks between between 135 and 125 ppm have larger intensities (Fig. 12b, inset). In general, the transfer is competitive with CP for the aromatic region.

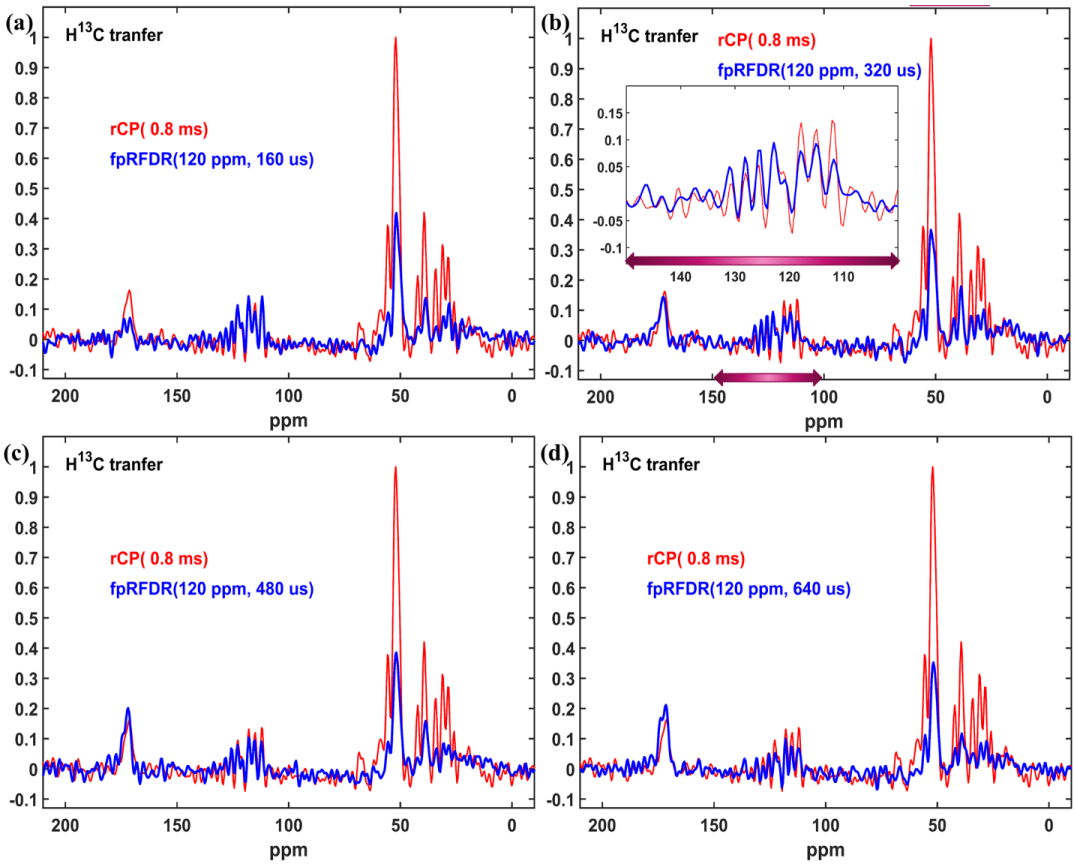

https://doi.org/10.5194/mr-2020-30
Preprint. Discussion started: 20 November 2020

Open Access MAGNETIC RESONANCE Discussions

Fig. 12 ^{13}C fpRFDR spectra recorded at different mixing times of 160 us (a), 320 us (b), 480 us (c) and 640 us (d) compared with 0.8 ms CP. The carbon reference frequency was set to 120 ppm. The expansion in (b) shows aromatic signals between 150 and 100 ppm. 100 kHz of MAS was used. The experimental parameters are shown in Table 3.

When the carbon reference frequency is set up on the 40 ppm (Fig. 13), the proton magnetization is mostly transferred to the aliphatic groups. Short mixing times result in optimal transfer.

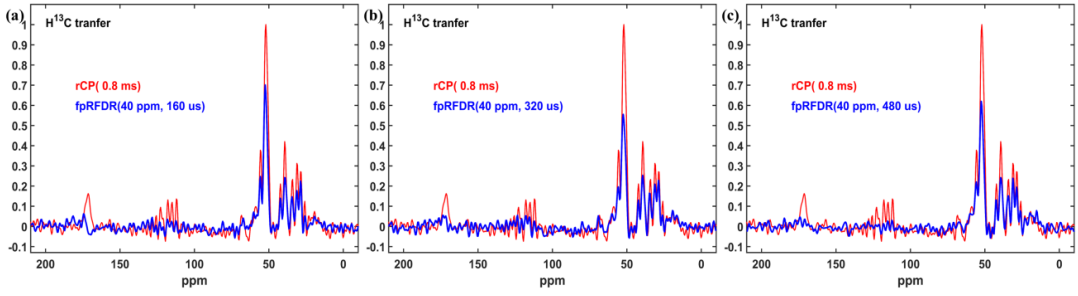

Fig. 13 ^{13}C fpRFDR spectra recorded at different mixing times: 160 us (a), 320 us (b) and 480 us (c) compared with 0.8 ms CP. The carbon reference frequency was set to 40 ppm. 100 kHz of MAS was used. The experimental parameters are shown in Table 3.

Fig. 14 shows 1D ^{1}H-{^{15}N} fp-RFDR spectra at different mixing times (thick blue lines), when the nitrogen reference frequence was set to 118 ppm. Red lines show a 1 ms ^{1}H-{^{15}N} CP spectrum. Optimal transfer occurs at around 400 microseconds.

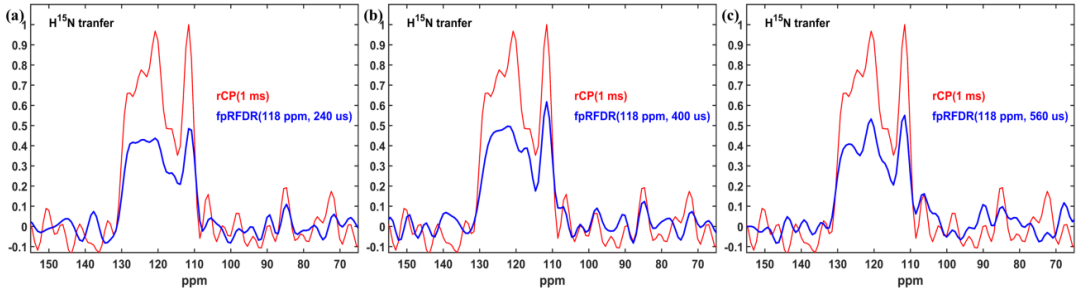

Fig. 14 ^{15}N fp-RFDR spectra at different mixing times: 240 us (a), 400 us (b) and 560 us (c) compared with 1 ms CP. The nitrogen reference frequency was set to 118 ppm. 100 kHz of MAS was used. The experimental parameters are shown in Table 4.

Conclusion

https://doi.org/10.5194/mr-2020-30
Preprint. Discussion started: 20 November 2020

The first RFDR experiment via a longitudinal exchange was demonstrated in 1992 by Bennet et all(A. E. Bennett et al. 1992). It has since become one of the routine MAS solid-state NMR mixing sequences. Using average Hamiltonian theory, the theoretical and the simulated descriptions of this sequence were demonstrated in many articles(A. E. Bennett et al. 1992; Ishii 2001; Nishiyama, Zhang, and Ramamoorthy 2014; R. Zhang et al. 2015; Brinkmann, Schmedt auf der Günne, and Levitt 2002; Ji et al. 2020). In those theoretical descriptions the width of the duty factor was considered as a main source of the fp-RFDR transferred signal, whereas a role of the phase cycling was discussed in the context of a reduction in deleterious effects of resonance offsets and pulse errors(A. E. Bennett et al. 1992; Ishii 2001). Through AHT, the evolution of the spin system under RFDR has been previously calculated at specific time points.

In this article we showed a numerical investigation of the fpRFDR sequence. Using a three spin system, we showed that depending on the conditions the total dipolar Hamiltonian could be replaced by two different simplified model Hamiltonians, which described the same evolution of the spin system at specific time points as a total dipolar Hamiltonian. For the first case, small differences between offset values compared with the MAS rate, a good model Hamiltonian was the secular part only, $I_{zr}I_{zs}$ (Eq. 2.2a). For the second case of larger offsets, the flip-flop Hamitonian (Eq. 2.2c) could be considered as a model Hamiltonian. The conclusion for the first case indicated the possibility for a heteronuclear fp-RFDR transfer. Heteronuclear fp-RFDR was demonstrated experimentally for both proton-carbon and proton-nitrogen transfer. While the transfer efficiency was not as high as for ramped CP, a comparable transfer efficiency was observed for aromatic signals. Since heteronuclear RFDR simultaneously recouples homonuclear dipolar interactions, it may still be useful where longer relayed transfers are desired.

Using two model spin systems we investigated the macroscopic amplitudes of the heteronuclear and homonuclear operators and showed that for small offset differences the evolution of the homonuclear and heteronuclear spin systems could be described with the same set of the operators with the same amplitudes, if one looks only at the end of two rotor periods. However, the evolutions of the homonuclear

https://doi.org/10.5194/mr-2020-30
Preprint. Discussion started: 20 November 2020

and heteronuclear operators were completely different, when their amplitudes were simulated within the 2 rotor period block.

We demonstrated with simulations and provided the theoretical proof that XY phase cycling of π-pulses has a crucial role in the transfer of the homonuclear and heteronuclear fp-RFDR signals. With phase cycling of XX or $X\overline{X}$ the fpRFDR transfer does not occur, except for cases when the offset differences are comparable with the MAS rate.

We considered the paths and the operators, which were involved in transfer of the signal during the first two rotor periods. For the heteronuclear spin system we found only one path with nonzero amplitude, whereas for the homonuclear spin system the signal was transferred via 64 paths with nonzero amplitudes. However, by the end of two rotor periods the amplitudes of the homonuclear operators coincided with the amplitudes of the heteronuclear operators.

Experimental methods

Sample preparation: 100% back bone protonated Transamination (α-PET SH3) was prepared by Movellan with the protocol described in Ref. [(Movellan et al. 2019)].

Simulations: RFDR simulations were performed with in-house MATLAB scripts using numerical solution of the experiment. The description of the simulations can be found in the '*Theory*' section of this article.

Solid state NMR spectroscopy: ramped CP and fp-RFDR H{^{13}C} / H{^{15}N} experiments were performed at a 22.3 T (950 MHz) Bruker Avance III spectrometer using a Bruker 0.7 mm ^{1}H-^{13}C-^{2}D-^{15}N probe. In all experiments 100 kHz of MAS was used and the temperature was set to 260 K. 18.5 kHz SW_f-TPPM (Thakur, Kurur, and Madhu 2006) with 25 us pulses was used during the acquisition. Tables 3 and 4 summarize the applied experimental parameters.

Table 3 Summary of the experimental parameters used in the rCP (the start and the end values are shown) and fpRFDR H{^{13}C} experiments.

https://doi.org/10.5194/mr-2020-30
Preprint. Discussion started: 20 November 2020

Open Access MAGNETIC RESONANCE Discussions

	CP	fpRFDR
^{1}H (kHz)	120-141	50.2
^{13}C (kHz)	28.4	47
transfer time	0.8 ms	160, 320, 480 µs
NS	1200	1200
D1 (s)	2	2
AQ (s)	0.02048	0.02048
SW (Hz)	100000	100000

NS – number of scans; D1 – a recycle delay; AQ – the acquisition time; SW – the spectral width.

Table 4 Summary of the experimental parameters used in the rCP (the start and the end values are shown) and fpRFDR H{^{15}N} experiments.

	rCP	fpRFDR
^{1}H (kHz)	118-139	50.2
^{15}N (kHz)	30.2	49.31
transfer time	1 ms	240, 400, 560 µs
NS	2000	2000
D1 (s)	10	10
AQ (s)	0.0135168	0.0135168
SW (Hz)	75757.58	75757.58

NS – Number Scans; D1 – a recycle delay; AQ – the acquisition time; SW – the spectral width.

Author Contributions

EN designed the project, performed the simulations, the experiments and wrote the article. KX took a part in the experiments and in the edition of the article. KTM prepared α-PET SH3 sample and packed it. LA contributed to the simulated and the experimental parts and edited the article.

Competing Interests

The authors declare that they have no conflict of interest.

Acknowledgments

We acknowledge financial support from the MPI for Biophysical Chemistry, and from the Deutsche Forschungsgemeinschaft (Emmy Noether program Grant AN1316/1- 1)

Appendix A

https://doi.org/10.5194/mr-2020-30
Preprint. Discussion started: 20 November 2020

Open Access MAGNETIC RESONANCE Discussions

Fig. A1 shows the fpRFDR signals of the I_3 (Fig. A1a and c) and IS_2 (Fig. A1b and d) spin systems obtaining with MATLAB simulations (solid lines) and SIMPSON simulations (grey dashed lines). MATLAB and SIMPSON simulated curves provide the same behavior of the starting and trasnferred signals under different experimental conditions: 10 kHz (Fig. A1a and b) and 90 kHz (Fig. A1 c and d) of MAS rates. IS_2 spin system contains the heteronuclear and homonuclear dipolar interactions, whereas I_3 spin system contains homonuclear dipolar interactions only. Under slow MAS rate of 10 kHz we detect low transferred signals between weakly bounded spins – I_{z2} and I_{z1} (black line) and I_{z3} and I_{z1} (purple line) for I_3 spin system (Fig. A1a) and much weaker signals for IS_2 spin system - S_{z2} and I_{z1} (black line) and S_{z3} and I_{z1} (purple line), Fig. A1b. However, under 90 kHz of MAS rate, the simulations provides the same results for I_3 (Fig. A1c) and IS_2 (Fig. A1d) spin systems.

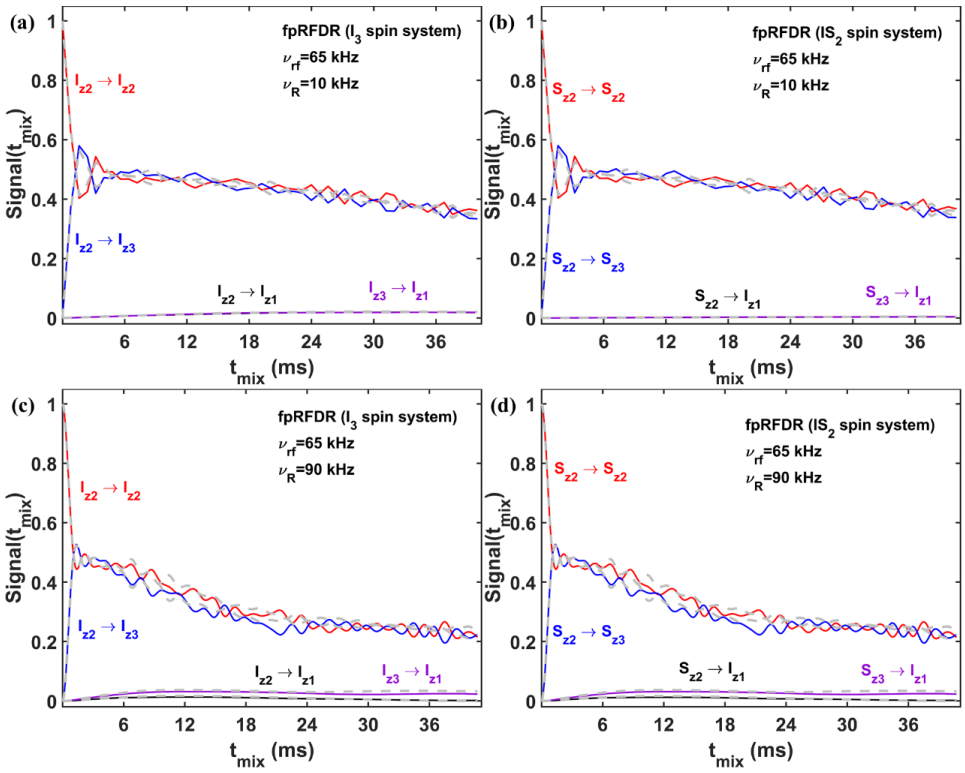

Fig. A1 Simulated I_3 (a, c) and IS_2 (b, d) spin systems under 10 kHz (a, b) and 90 kHz (c, d) of MAS with 65 kHz of rf-field, dipolar values of $\nu_{12} = 66$ Hz, $\nu_{13} = 150$ Hz, $\nu_{23} = 2.15$ kHz, the offset values of $\Omega_1 = -8$ kHz, $\Omega_2 = 9$ kHz, $\Omega_3 = -7$ kHz

https://doi.org/10.5194/mr-2020-30
Preprint. Discussion started: 20 November 2020

and CSA values of $\nu_{CSA,1} = 9.2$ Hz, f $\nu_{CSA,2} = 2.5$ Hz, f $\nu_{CSA,3} = 8$ kHz. The solid lines represent fp-RFDR starting and transferred signals obtaining with MATLAB simulations, whereas the dashed signals were obtained with SIMPSON simulations. (a), (c): : $I_{z2} \rightarrow I_{z2}$ (red lines); $I_{z2} \rightarrow I_{z3}$ (blue lines); $I_{z2} \rightarrow I_{z1}$ (black lines); $I_{z3} \rightarrow I_{z1}$ (purple lines). (b), (d): $S_{z2} \rightarrow S_{z2}$ (red lines); $S_{z2} \rightarrow S_{z3}$ (blue lines); $S_{z2} \rightarrow I_{z1}$ (black lines); $S_{z3} \rightarrow I_{z1}$ (purple lines). The values of the dipolar interactions and 10 kHz of MAS was taken from Ref. [(Bayro et al. 2009)]. XY8 phase cycling was used.

Fig A2 compares the starting and transferred signals obtained with the full dipolar Hamiltonian (Eq. 2.1) or simulating with the secular dipolar Hamiltonian (Eq. 2.2a), when CSA values (Fig. A2a) or offset values (Fig. A2b) are added to the simulations. The CSA values themselves (Fig. A2a) have very small influence on the evolution of the spin system and therefore the secular dipolar Hamiltonian (red lines) provides the same evolution of the spin system as the full dipolar Hamiltonian (black lines). The main influence comes from offset values as shown in Fig. A2b. Under these conditions, the red and black lines do not coinside.

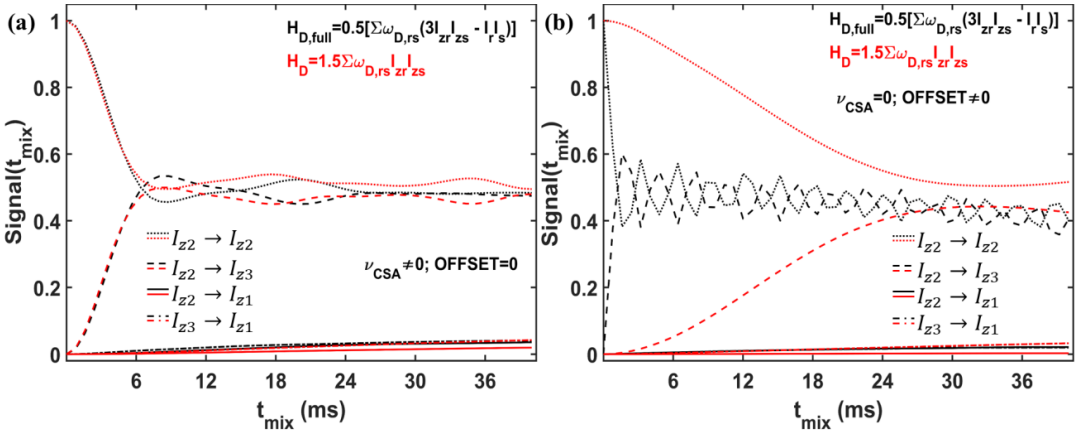

Fig. A2 Simulated I_3 spin system under 10 kHz of MAS and 65 kHz of rf-field, dipolar coupling values of $\nu_{12} = 66$ Hz, $\nu_{13} = 150$ Hz, $\nu_{23} = 2.15$ kHz. Axis Y shows the intensities of the starting and transferred signals between different operators: $I_{z2} \rightarrow I_{z2}$ (the dotted lines); $I_{z2} \rightarrow I_{z3}$ (the dashed lines); $I_{z2} \rightarrow I_{z1}$ (the solid lines); $I_{z3} \rightarrow I_{z1}$ (the dashed-dotted lines). The black lines represent the signals, simulating with the full dipolar Hamiltonian (Eq. 2.1) with zero values of offset and CSA. The red lines represent the signals, simulating with the secular model Hamiltonian (Eq. 2.2a). (a) Offset values: 0; CSA values: $\nu_{CSA,1} = 9.2$ Hz, f $\nu_{CSA,2} = 2.5$ Hz, f $\nu_{CSA,3} = 8$ kHz. (b) $\Omega_1 = -8$ kHz, $\Omega_2 = 9$ kHz, $\Omega_3 = -7$ kHz; CSA values: 0.

https://doi.org/10.5194/mr-2020-30
Preprint. Discussion started: 20 November 2020

Appendix B

For the theoretical proof of zero fpRFDR signal at specific time points when XX phase cycling is used, we can consider the transfer of the signal from spin I_1 to spin I_2 at the end of one rotor period. The measured operator at this time is described with the Eqn.:

$$\langle I_{z2}\rangle(T_R) = Tr\{I_{z2}U(T_R)I_{z1}U^{-1}(T_R)\}. \tag{B1}$$

For simplicity, we take into account the dipolar interaction + rf-field during π-pulse and the dipolar interaction only during the delay. In that case the unitary operator, $U(T_R)$ is written as follow:

$$U(T_R) = U_2U_1: \quad \begin{matrix} U_2 = \hat{T}exp\left\{\int_{t_p}^{T_R} dt\omega_{D,12}(t)(3I_{z1}I_{z2} - \bar{I}_1\bar{I}_2)\right\} \\ U_1 = \hat{T}exp\left\{\int_0^{t_p} dt\left[\omega_{D,12}(t)(3I_{z1}I_{z2} - \bar{I}_1\bar{I}_2) + \omega_{rf}(I_{x1} + I_{x2})\right]\right\} \end{matrix}, \tag{B2}$$

where $\hat{T}$ is a Dyson operator and $\omega_{D,12}(t)$ is a periodic dipolar time dependent function(Olejniczak, Vega, and Griffin 1984) between spins I_1 and I_2. Firstly, we can simplify Eq. B2 omitting the scalar product, $\bar{I}_1\bar{I}_2$, since it communicates with other parts of the Hamiltonian:

$$[\bar{I}_1\bar{I}_2, I_{z1}I_{z2}] = [\bar{I}_1\bar{I}_2, I_{x1} + I_{x2}] = 0, \tag{B3}$$

and the dipolar function is periodic – $\int_0^{T_R} dt\omega_{D,12}(t)\bar{I}_1\bar{I}_2 = 0$. Eq. B2 can be written as follow:

$$U(T_R) = U_2U_1: \quad \begin{matrix} U_2 = \hat{T}exp\left\{\int_{t_p}^{T_R} dt\omega_{D,12}(t)3I_{z1}I_{z2}\right\} \\ U_1 = \hat{T}exp\left\{\int_0^{t_p} dt\left[\omega_{D,12}(t)3I_{z1}I_{z2} + \omega_{rf}(I_{x1} + I_{x2})\right]\right\} \end{matrix}, \tag{B4}$$

The next step is the rotation of the all operators by 90° around axis -y:

$$I_{z1}, I_{z2}, I_{z1}I_{z2}, (I_{x1} + I_{x2}) \xrightarrow{90-y} -I_{x1}, -I_{x2}, I_{x1}I_{x2}, (I_{z1} + I_{z2}). \tag{B5}$$

Substituting Eq. B5 into Eqs. B1 and B4, the modified Eq. B1 is:

$$\langle I_{z2}\rangle(T_R) = Tr\{I_{x2}U(T_R)I_{x1}U^{-1}(T_R)\}, \tag{B6}$$

whereas the modified Eq. B4 is:

https://doi.org/10.5194/mr-2020-30
Preprint. Discussion started: 20 November 2020

Open Access MAGNETIC RESONANCE Discussions

$$U(T_R) = U_2 U_1: \begin{array}{c} U_2 = \hat{T} exp\left\{\int_{t_p}^{T_R} dt \omega_{D,12}(t) 3 I_{x1} I_{x2}\right\} \\ U_1 = \hat{T} exp\left\{\int_0^{t_p} dt \left[\omega_{D,12}(t) 3 I_{x1} I_{x2} + \omega_{rf}(I_{z1} + I_{z2})\right]\right\} \end{array}, \tag{B7}$$

The operators in Eqs. B6 and B7 can be rewritten with fictitious spin ½ operator formalism(Vega 1978):

$$\begin{array}{c} 2 I_{x1} I_{x2} = I_x^{(1,4)} + I_x^{(2,3)}, \\ (I_{z1} + I_{z2}) = 2 I_z^{(1,4)} \end{array}. \tag{B8}$$

Therefore, Eqs. B6 and B7 can be written as follow:

$$\langle I_{z2} \rangle (T_R) = Tr\{I_{x2} U(T_R) I_{x1} U^{-1}(T_R)\}, \tag{B9}$$

$$U(T_R) = U_2 U_1: \begin{array}{c} U_2 = \hat{T} exp\left\{\int_{t_p}^{T_R} dt \omega_{D,12}(t) 3 \left(I_x^{(1,4)} + I_x^{(2,3)}\right)\right\} \\ U_1 = \hat{T} exp\left\{\int_0^{t_p} dt \left[\omega_{D,12}(t) 3 \left(I_x^{(1,4)} + I_x^{(2,3)}\right) + \omega_{rf} 2 I_z^{(1,4)}\right]\right\} \end{array}. \tag{B10}$$

Since the operator $I_x^{(2,3)}$ communicates with other operators and the dipolar function is periodic – $\int_0^{T_R} dt \omega_{D,12}(t) I_x^{(2,3)} = 0$ – the Eqs. B9 and B10 can be rewritten as:

$$\langle I_{z2} \rangle (T_R) = Tr\left\{I_{x2} U^{(1,4)}(T_R) I_{x1} \left(U^{(1,4)}\right)^{-1}(T_R)\right\}, \tag{B9}$$

$$U^{(1,4)}(T_R) = U_2^{(1,4)} U_1^{(1,4)}: \begin{array}{c} U_2^{(1,4)} = \hat{T} exp\left\{\int_{t_p}^{T_R} dt \omega_{D,12}(t) 3 I_x^{(1,4)}\right\} \\ U_1^{(1,4)} = \hat{T} exp\left\{\int_0^{t_p} dt \left[\omega_{D,12}(t) 3 I_x^{(1,4)} + \omega_{rf} 2 I_z^{(1,4)}\right]\right\} \end{array}. \tag{B10}$$

On the basis of the fictitious spin ½ operator formalism(Vega 1978), the next properties are always performed:

$$\begin{array}{c} 2 I_{xj} I_x^{(1,4)} 2 I_{xj} = I_x^{(2,3)}, \\ 2 I_{xj} I_z^{(1,4)} 2 I_{xj} = -I_z^{(2,3)}, \qquad \mathrm{j} = 1,2. \end{array} \tag{B11}$$

On the basis of these properties Eqs. B9 and B10 are:

$$\langle I_{z2} \rangle (T_R) = Tr\left\{I_{x2} I_{x1} \breve{U}^{(2,3)}(T_R) \left(U^{(1,4)}\right)^{-1}(T_R)\right\}, \tag{B12}$$

$$\breve{U}^{(2,3)}(T_R) = \breve{U}_2^{(2,3)} \breve{U}_1^{(2,3)}: \begin{array}{c} \breve{U}_2^{(2,3)} = \hat{T} exp\left\{\int_{t_p}^{T_R} dt \omega_{D,12}(t) 3 I_x^{(2,3)}\right\} \\ \breve{U}_1^{(2,3)} = \hat{T} exp\left\{\int_0^{t_p} dt \left[\omega_{D,12}(t) 3 I_x^{(2,3)} - \omega_{rf} 2 I_z^{(2,3)}\right]\right\} \end{array}. \tag{B13}$$

On the basic of Eq. B8 the product of $I_{x2} I_{x1}$ can be rewritten and therefore Eq. B12 is:

https://doi.org/10.5194/mr-2020-30
Preprint. Discussion started: 20 November 2020

Open Access MAGNETIC RESONANCE Discussions

$$\langle I_{z2}\rangle(T_R) = 0.5Tr\left\{\left(I_x^{(1,4)} + I_x^{(2,3)}\right)\breve{U}^{(2,3)}(T_R)\left(U^{(1,4)}\right)^{-1}(T_R)\right\} =$$
$$=0.5Tr\left\{I_x^{(2,3)}\breve{U}^{(2,3)}(T_R)\right\} + 0.5Tr\left\{I_x^{(1,4)}\left(U^{(1,4)}\right)^{-1}(T_R)\right\}. \quad \text{(B14)}$$

The next step will be usage of the mentioned properties of fictitious spin ½ operator formalism (Eq. B11):

$$\langle I_{z2}\rangle(T_R) = 0.5Tr\left\{I_x^{(2,3)}\breve{U}^{(2,3)}(T_R)\right\} + 0.5Tr\left\{I_x^{(2,3)}\left(\breve{U}^{(2,3)}\right)^{-1}(T_R)\right\}. \quad \text{(B15)}$$

The last step will be the usage the next property:

$$-2I_y^{(2,3)}I_x^{(2,3)}2I_y^{(2,3)} = I_x^{(2,3)},$$
$$-2I_y^{(2,3)}I_z^{(2,3)}2I_y^{(2,3)} = I_z^{(2,3)}. \quad \text{(B16)}$$

Substituting Eq. B11 into Eq. B13, then the modified Eq. B13 into Eq. B15 and taking into account that $2I_y^{(2,3)}2I_y^{(2,3)} = 1^{(2,3)}$, the transferred signal is:

$$\langle I_{z2}\rangle(T_R) = -0.5Tr\left\{I_x^{(2,3)}\left(\breve{U}^{(2,3)}\right)^{-1}(T_R)\right\} + 0.5Tr\left\{I_x^{(2,3)}\left(\breve{U}^{(2,3)}\right)^{-1}(T_R)\right\} = 0. \quad \text{(B17)}$$

Since the transferred signal is zero at mixing the time of one rotor period, it is always zero at integer multiples of rotor periods.

Andreas, Loren B., Tanguy Le Marchand, Kristaps Jaudzems, and Guido Pintacuda. 2015. "High-Resolution Proton-Detected NMR of Proteins at Very Fast MAS." *Journal of Magnetic Resonance*, Special Issue: Recent Achievements and New Directions in Biomolecular Solid State NMR, 253 (April): 36–49. https://doi.org/10.1016/j.jmr.2015.01.003.

Aucoin, Darryl, Devin Camenares, Xin Zhao, Jay Jung, Takeshi Sato, and Steven O. Smith. 2009. "High Resolution 1H MAS RFDR NMR of Biological Membranes." *Journal of Magnetic Resonance (San Diego, Calif. : 1997)* 197 (1): 77–86. https://doi.org/10.1016/j.jmr.2008.12.009.

Bak, M., J. T. Rasmussen, and N. C. Nielsen. 2000. "SIMPSON : A General Simulation Program for Solid-State NMR Spectroscopy." *Journal of Magnetic Resonance (San Diego, Calif. : 1997)*, 1–35. https://doi.org/10.1006/jmre.2000.2179.

Bayro, Marvin J., Matthias Huber, Ramesh Ramachandran, Timothy C. Davenport, Beat H. Meier, Matthias Ernst, and Robert G. Griffin. 2009. "Dipolar Truncation in Magic-Angle Spinning NMR Recoupling Experiments." *The Journal of Chemical Physics* 130 (11). https://doi.org/10.1063/1.3089370.

https://doi.org/10.5194/mr-2020-30
Preprint. Discussion started: 20 November 2020

Bennett, A. E., R. G. Griffin, J. H. Ok, and S. Vega. 1992. "Chemical Shift Correlation Spectroscopy in Rotating Solids: Radio Frequency-driven Dipolar Recoupling and Longitudinal Exchange." *The Journal of Chemical Physics* 96 (11): 8624–27. https://doi.org/10.1063/1.462267.

Bennett, Andrew E., Chad M. Rienstra, Janet M. Griffiths, Weiguo Zhen, Peter T. Lansbury, and Robert G. Griffin. 1998. "Homonuclear Radio Frequency-Driven Recoupling in Rotating Solids." *The Journal of Chemical Physics* 108 (22): 9463–79. https://doi.org/10.1063/1.476420.

Brinkmann, Andreas, and Malcolm H. Levitt. 2001. "Symmetry Principles in the Nuclear Magnetic Resonance of Spinning Solids: Heteronuclear Recoupling by Generalized Hartmann–Hahn Sequences." *The Journal of Chemical Physics* 115 (1): 357–84. https://doi.org/10.1063/1.1377031.

Brinkmann, Andreas, Jörn Schmedt auf der Günne, and Malcolm H. Levitt. 2002. "Homonuclear Zero-Quantum Recoupling in Fast Magic-Angle Spinning Nuclear Magnetic Resonance." *Journal of Magnetic Resonance* 156 (1): 79–96. https://doi.org/10.1006/jmre.2002.2525.

Carravetta, Marina, Mattias Edén, Xin Zhao, Andreas Brinkmann, and Malcolm H Levitt. 2000. "Symmetry Principles for the Design of Radiofrequency Pulse Sequences in the Nuclear Magnetic Resonance of Rotating Solids." *Chemical Physics Letters* 321 (3): 205–15. https://doi.org/10.1016/S0009-2614(00)00340-7.

Colvin, Michael T., Robert Silvers, Birgitta Frohm, Yongchao Su, Sara Linse, and Robert G. Griffin. 2015. "High Resolution Structural Characterization of Aβ42 Amyloid Fibrils by Magic Angle Spinning NMR." *Journal of the American Chemical Society* 137 (23): 7509–18. https://doi.org/10.1021/jacs.5b03997.

Daskalov, A., D. Martinez, V. Coustou, N. El Mammeri, M. Berbon, L. B. Andreas, B. Bardiaux, et al. 2020. "Structural and Molecular Basis of Cross-Seeding Barriers in Amyloids." *BioRxiv*, July, 2020.07.06.188508. https://doi.org/10.1101/2020.07.06.188508.

Ernst, R.R., G. Bodenhausen, and A. Wokaun. 1987. *Principles of Nuclear Magnetic Resonance in One and Two Dimensions*. Oxford Univ. Press, London/New York. https://onlinelibrary.wiley.com/doi/abs/10.1002/mrm.1910070215.

Fritz, Matthew, Jodi Kraus, Caitlin M. Quinn, Glenn P. A. Yap, Jochem Struppe, Ivan V. Sergeyev, Angela M. Gronenborn, and Tatyana Polenova. 2019. "Measurement of Accurate Interfluorine Distances in Crystalline Organic Solids: A High-Frequency Magic Angle Spinning NMR Approach." *The Journal of Physical Chemistry B* 123 (50): 10680–90. https://doi.org/10.1021/acs.jpcb.9b08919.

Gelenter, Martin D., Aurelio J. Dregni, and Mei Hong. 2020. "Pulsed Third-Spin-Assisted Recoupling NMR for Obtaining Long-Range 13C–13C and 15N–13C Distance Restraints." *The Journal of Physical Chemistry B* 124 (33): 7138–51. https://doi.org/10.1021/acs.jpcb.0c04574.

Gelenter, Martin D., and Mei Hong. 2018. "Efficient 15N–13C Polarization Transfer by Third-Spin-Assisted Pulsed Cross-Polarization Magic-Angle-Spinning NMR for Protein Structure Determination." *The Journal of Physical Chemistry B* 122 (35): 8367–79. https://doi.org/10.1021/acs.jpcb.8b06400.

Grohe, Kristof, Evgeny Nimerovsky, Himanshu Singh, Suresh K. Vasa, Benedikt Söldner, Beat Voegeli, Chad M. Rienstra, and Rasmus Linser. 2019. "Exact Distance Measurements for Structure and Dynamics in Solid Proteins by Fast-Magic-Angle-Spinning NMR." *Chemical Communications*, June. https://doi.org/10.1039/C9CC02317H.

Gullion, T., and J. Schaefer. 1989. "Rotational-Echo Double-Resonance NMR." *Journal of Magnetic Resonance (1969)* 81 (1): 196–200. https://doi.org/10.1016/0022-2364(89)90280-1.

Gullion, Terry, David B Baker, and Mark S Conradi. 1990. "New, Compensated Carr-Purcell Sequences." *Journal of Magnetic Resonance (1969)* 89 (3): 479–84. https://doi.org/10.1016/0022-2364(90)90331-3.

https://doi.org/10.5194/mr-2020-30
Preprint. Discussion started: 20 November 2020

Gullion, Terry, and Shimon Vega. 1992. "A Simple Magic Angle Spinning NMR Experiment for the Dephasing of Rotational Echoes of Dipolar Coupled Homonuclear Spin Pairs." *Chemical Physics Letters* 194 (4): 423–28. https://doi.org/10.1016/0009-2614(92)86076-T.

Haeberlen, U., and J. S. Waugh. 1968. "Coherent Averaging Effect in Magnetic Resonance." *Physical Review* 175 (2): 453–467. https://doi.org/10.1103/PhysRev.175.453.

Hartmann, S. R., and E. L. Hahn. 1962. "Nuclear Double Resonance in the Rotating Frame." *Physical Review* 128 (5): 2042–53. https://doi.org/10.1103/PhysRev.128.2042.

Hediger, S., B. H. Meier, Narayanan D. Kurur, Geoffrey Bodenhausen, and R. R. Ernst. 1994. "NMR Cross Polarization by Adiabatic Passage through the Hartmann—Hahn Condition (APHH)." *Chemical Physics Letters* 223 (4): 283–88. https://doi.org/10.1016/0009-2614(94)00470-6.

Hellwagner, Johannes, Nino Wili, Luis Fábregas Ibáñez, Johannes J. Wittmann, Beat H. Meier, and Matthias Ernst. 2018. "Transient Effects in π-Pulse Sequences in MAS Solid-State NMR." *Journal of Magnetic Resonance* 287 (February): 65–73. https://doi.org/10.1016/j.jmr.2017.12.015.

Hing, Andrew W, Shimon Vega, and Jacob Schaefer. 1992. "Transferred-Echo Double-Resonance NMR." *Journal of Magnetic Resonance (1969)* 96 (1): 205–9. https://doi.org/10.1016/0022-2364(92)90305-Q.

Hou, Guangjin, In-Ja L. Byeon, Jinwoo Ahn, Angela M. Gronenborn, and Tatyana Polenova. 2011. "1H–13C/1H–15N Heteronuclear Dipolar Recoupling by R-Symmetry Sequences Under Fast Magic Angle Spinning for Dynamics Analysis of Biological and Organic Solids." *Journal of the American Chemical Society* 133 (46): 18646–55. https://doi.org/10.1021/ja203771a.

Hou, Guangjin, Si Yan, Shangjin Sun, Yun Han, In-Ja L. Byeon, Jinwoo Ahn, Jason Concel, Ago Samoson, Angela M. Gronenborn, and Tatyana Polenova. 2011. "Spin Diffusion Driven by R-Symmetry Sequences: Applications to Homonuclear Correlation Spectroscopy in MAS NMR of Biological and Organic Solids." *Journal of the American Chemical Society* 133 (11): 3943–53. https://doi.org/10.1021/ja108650x.

Hou, Guangjin, Si Yan, Julien Trébosc, Jean-Paul Amoureux, and Tatyana Polenova. 2013. "Broadband Homonuclear Correlation Spectroscopy Driven by Combined R2nv Sequences under Fast Magic Angle Spinning for NMR Structural Analysis of Organic and Biological Solids." *Journal of Magnetic Resonance* 232 (July): 18–30. https://doi.org/10.1016/j.jmr.2013.04.009.

Ishii, Yoshitaka. 2001. "13C–13C Dipolar Recoupling under Very Fast Magic Angle Spinning in Solid-State Nuclear Magnetic Resonance: Applications to Distance Measurements, Spectral Assignments, and High-Throughput Secondary-Structure Determination." *The Journal of Chemical Physics* 114 (19): 8473–83. https://doi.org/10.1063/1.1359445.

Jain, Mukul G., Daniela Lalli, Jan Stanek, Chandrakala Gowda, Satya Prakash, Tom S. Schwarzer, Tobias Schubeis, et al. 2017. "Selective 1H–1H Distance Restraints in Fully Protonated Proteins by Very Fast Magic-Angle Spinning Solid-State NMR." *The Journal of Physical Chemistry Letters* 8 (11): 2399–2405. https://doi.org/10.1021/acs.jpclett.7b00983.

Jaroniec, Christopher P., Claudiu Filip, and Robert G. Griffin. 2002. "3D TEDOR NMR Experiments for the Simultaneous Measurement of Multiple Carbon−Nitrogen Distances in Uniformly 13C,15N-Labeled Solids." *Journal of the American Chemical Society* 124 (36): 10728–42. https://doi.org/10.1021/ja026385y.

Ji, Yi, Lixing Liang, Changmiao Guo, Xinhe Bao, Tatyana Polenova, and Guangjin Hou. 2020. "Zero-Quantum Homonuclear Recoupling Symmetry Sequences in Solid-State Fast MAS NMR Spectroscopy." *Acta Physico-Chimica Sinica* 36 (4): 1905029–34.

Levante, T. O., M. Baldus, B. H. Meier, and R. R. Ernst. 1995. "Formalized Quantum Mechanical Floquet Theory and Its Application to Sample Spinning in Nuclear Magnetic Resonance." *Molecular Physics* 86 (5): 1195–1212. https://doi.org/10.1080/00268979500102671.

https://doi.org/10.5194/mr-2020-30
Preprint. Discussion started: 20 November 2020

Maricq, M. M. 1982. "Application of Average Hamiltonian Theory to the NMR of Solids." *Physical Review B* 25 (11): 6622–6632. https://doi.org/10.1103/PhysRevB.25.6622.

Messinger, Robert J., Michel Ménétrier, Elodie Salager, Adrien Boulineau, Mathieu Duttine, Dany Carlier, Jean-Marcel Ateba Mba, et al. 2015. "Revealing Defects in Crystalline Lithium-Ion Battery Electrodes by Solid-State NMR: Applications to LiVPO4F." *Chemistry of Materials* 27 (15): 5212–21. https://doi.org/10.1021/acs.chemmater.5b01234.

Metz, G., X. L. Wu, and S. O. Smith. 1994. "Ramped-Amplitude Cross Polarization in Magic-Angle-Spinning NMR." *Journal of Magnetic Resonance, Series A* 110 (2): 219–27. https://doi.org/10.1006/jmra.1994.1208.

Movellan, Kumar Tekwani, Eszter E. Najbauer, Supriya Pratihar, Michele Salvi, Karin Giller, Stefan Becker, and Loren B. Andreas. 2019. "Alpha Protons as NMR Probes in Deuterated Proteins." *Journal of Biomolecular NMR* 73 (1): 81–91. https://doi.org/10.1007/s10858-019-00230-y.

Nielsen, N. C., H. Bildso/e, H. J. Jakobsen, and M. H. Levitt. 1994. "Double-quantum Homonuclear Rotary Resonance: Efficient Dipolar Recovery in Magic-angle Spinning Nuclear Magnetic Resonance." *The Journal of Chemical Physics* 101 (3): 1805–12. https://doi.org/10.1063/1.467759.

Nimerovsky, E., and A. Goldbourt. 2012. "Insights into the Spin Dynamics of a Large Anisotropy Spin Subjected to Long-Pulse Irradiation under a Modified REDOR Experiment." *Journal of Magnetic Resonance* 225: 130–41. https://doi.org/10.1016/j.jmr.2012.09.015.

Nishiyama, Yusuke, Michal Malon, Yuji Ishii, and Ayyalusamy Ramamoorthy. 2014. "3D 15N/15N/1H Chemical Shift Correlation Experiment Utilizing an RFDR-Based 1H/1H Mixing Period at 100kHz MAS." *Journal of Magnetic Resonance* 244 (July): 1–5. https://doi.org/10.1016/j.jmr.2014.04.008.

Nishiyama, Yusuke, Rongchun Zhang, and Ayyalusamy Ramamoorthy. 2014. "Finite-Pulse Radio Frequency Driven Recoupling with Phase Cycling for 2D 1H/1H Correlation at Ultrafast MAS Frequencies." *Journal of Magnetic Resonance* 243 (June): 25–32. https://doi.org/10.1016/j.jmr.2014.03.004.

Ok, J. H., R. G. S. Spencer, A. E. Bennett, and R. G. Griffin. 1992. "Homonuclear Correlation Spectroscopy in Rotating Solids." *Chemical Physics Letters* 197 (4): 389–95. https://doi.org/10.1016/0009-2614(92)85790-H.

Olejniczak, E. T., S. Vega, and R. G. Griffin. 1984. "Multiple Pulse NMR in Rotating Solids." *The Journal of Chemical Physics* 81 (11): 4804–17. https://doi.org/10.1063/1.447506.

Pandey, Manoj Kumar, and Yusuke Nishiyama. 2018. "A One-Dimensional Solid-State NMR Approach for 14NH/14NH Overtone Correlation through 1H/1H Mixing under Fast MAS." *Physical Chemistry Chemical Physics* 20 (40): 25849–53. https://doi.org/10.1039/C8CP05000G.

Pandey, Manoj Kumar, Subramanian Vivekanandan, Kazutoshi Yamamoto, Sangchoul Im, Lucy Waskell, and Ayyalusamy Ramamoorthy. 2014. "Proton-Detected 2D Radio Frequency Driven Recoupling Solid-State NMR Studies on Micelle-Associated Cytochrome-B5." *Journal of Magnetic Resonance* 242 (May): 169–79. https://doi.org/10.1016/j.jmr.2014.02.016.

Petkova, A. T., Y. Ishii, J. J. Balbach, O. N. Antzutkin, R. D. Leapman, F. Delaglio, and R. Tycko. 2002. "A Structural Model for Alzheimer's -Amyloid Fibrils Based on Experimental Constraints from Solid State NMR." *Proceedings of the National Academy of Sciences* 99 (26): 16742–47. https://doi.org/10.1073/pnas.262663499.

Roos, Matthias, Venkata S. Mandala, and Mei Hong. 2018. "Determination of Long-Range Distances by Fast Magic-Angle-Spinning Radiofrequency-Driven 19F–19F Dipolar Recoupling NMR." *The Journal of Physical Chemistry B* 122 (40): 9302–13. https://doi.org/10.1021/acs.jpcb.8b06878.

Rovnyak, David. 2008. "Tutorial on Analytic Theory for Cross-Polarization in Solid State NMR." *Concepts in Magnetic Resonance Part A* 32A (4): 254–76. https://doi.org/10.1002/cmr.a.20115.

https://doi.org/10.5194/mr-2020-30
Preprint. Discussion started: 20 November 2020

Saalwächter, Kay. 2013. "Robust NMR Approaches for the Determination of Homonuclear Dipole–Dipole Coupling Constants in Studies of Solid Materials and Biomolecules." *ChemPhysChem* 14 (13): 3000–3014. https://doi.org/10.1002/cphc.201300254.

Scholz, Ingo, Jacco D. van Beek, and Matthias Ernst. 2010. "Operator-Based Floquet Theory in Solid-State NMR." *Solid State Nuclear Magnetic Resonance* 37 (3): 39–59. https://doi.org/10.1016/j.ssnmr.2010.04.003.

Shen, Ming, Bingwen Hu, Oliver Lafon, Julien Trébosc, Qun Chen, and Jean-Paul Amoureux. 2012. "Broadband Finite-Pulse Radio-Frequency-Driven Recoupling (Fp-RFDR) with (XY8)41 Super-Cycling for Homo-Nuclear Correlations in Very High Magnetic Fields at Fast and Ultra-Fast MAS Frequencies." *Journal of Magnetic Resonance* 223 (October): 107–19. https://doi.org/10.1016/j.jmr.2012.07.013.

Shi, Chaowei, Pascal Fricke, Lin Lin, Veniamin Chevelkov, Melanie Wegstroth, Karin Giller, Stefan Becker, Martin Thanbichler, and Adam Lange. 2015. "Atomic-Resolution Structure of Cytoskeletal Bactofilin by Solid-State NMR." *Science Advances* 1 (11). https://doi.org/10.1126/sciadv.1501087.

Slichter, Charles P. 1990. *Principles of Magnetic Resonance*. 3rd ed. Springer Series in Solid-State Sciences. Berlin Heidelberg: Springer-Verlag. https://doi.org/10.1007/978-3-662-09441-9.

Sodickson, D. K., M. H. Levitt, S. Vega, and R. G. Griffin. 1993. "Broad Band Dipolar Recoupling in the Nuclear Magnetic Resonance of Rotating Solids." *The Journal of Chemical Physics* 98 (9): 6742–48. https://doi.org/10.1063/1.464766.

Straasø, Lasse A., Ravi Shankar, Kong Ooi Tan, Johannes Hellwagner, Beat H. Meier, Michael Ryan Hansen, Niels Chr. Nielsen, Thomas Vosegaard, Matthias Ernst, and Anders B. Nielsen. 2016. "Improved Transfer Efficiencies in Radio-Frequency-Driven Recoupling Solid-State NMR by Adiabatic Sweep through the Dipolar Recoupling Condition." *The Journal of Chemical Physics* 145 (3): 034201. https://doi.org/10.1063/1.4958318.

Szeverenyi, Nikolaus M, Mark J Sullivan, and Gary E Maciel. 1982. "Observation of Spin Exchange by Two-Dimensional Fourier Transform 13C Cross Polarization-Magic-Angle Spinning." *Journal of Magnetic Resonance (1969)* 47 (3): 462–75. https://doi.org/10.1016/0022-2364(82)90213-X.

Takegoshi, K., Shinji Nakamura, and Takehiko Terao. 2001. "13C–1H Dipolar-Assisted Rotational Resonance in Magic-Angle Spinning NMR." *Chemical Physics Letters* 344 (5): 631–37. https://doi.org/10.1016/S0009-2614(01)00791-6.

Tang, Ming, Deborah A. Berthold, and Chad M. Rienstra. 2011. "Solid-State NMR of a Large Membrane Protein by Paramagnetic Relaxation Enhancement." *The Journal of Physical Chemistry Letters* 2 (14): 1836–41. https://doi.org/10.1021/jz200768r.

Thakur, Rajendra Singh, Narayanan D. Kurur, and P. K. Madhu. 2006. "Swept-Frequency Two-Pulse Phase Modulation for Heteronuclear Dipolar Decoupling in Solid-State NMR." *Chemical Physics Letters* 426 (4): 459–63. https://doi.org/10.1016/j.cplett.2006.06.007.

Vega, Shimon. 1978. "Fictitious Spin 1/2 Operator Formalism for Multiple Quantum NMR." *The Journal of Chemical Physics* 68 (12): 5518–27. https://doi.org/10.1063/1.435679.

Wong, Kong M., Yiming Wang, Dillon T. Seroski, Grant E. Larkin, Anil K. Mehta, Gregory A. Hudalla, Carol K. Hall, and Anant K. Paravastu. 2020. "Molecular Complementarity and Structural Heterogeneity within Co-Assembled Peptide β-Sheet Nanofibers." *Nanoscale* 12 (7): 4506–18. https://doi.org/10.1039/C9NR08725G.

Zhang, Rongchun, Kamal H. Mroue, and Ayyalusamy Ramamoorthy. 2017. "Proton-Based Ultrafast Magic Angle Spinning Solid-State NMR Spectroscopy." *Accounts of Chemical Research* 50 (4): 1105–13. https://doi.org/10.1021/acs.accounts.7b00082.

https://doi.org/10.5194/mr-2020-30
Preprint. Discussion started: 20 November 2020

Open Access MAGNETIC RESONANCE Discussions

Zhang, Rongchun, Yusuke Nishiyama, Pingchuan Sun, and Ayyalusamy Ramamoorthy. 2015. "Phase Cycling Schemes for Finite-Pulse-RFDR MAS Solid State NMR Experiments." *Journal of Magnetic Resonance* 252 (March): 55–66. https://doi.org/10.1016/j.jmr.2014.12.010.

Zhang, Zhengfeng, Yanke Chen, and Jun Yang. 2016. "Band-Selective Heteronuclear Dipolar Recoupling with Dual Back-to-Back Pulses in Rotating Solids." *Journal of Magnetic Resonance* 272 (November): 46–52. https://doi.org/10.1016/j.jmr.2016.09.003.

Zhang, Zhengfeng, Andres Oss, Mai-Liis Org, Ago Samoson, Mingyue Li, Huan Tan, Yongchao Su, and Jun Yang. 2020. "Selectively Enhanced 1H–1H Correlations in Proton-Detected Solid-State NMR under Ultrafast MAS Conditions." *The Journal of Physical Chemistry Letters* 11 (19): 8077–83. https://doi.org/10.1021/acs.jpclett.0c02412.

Zheng, Zhaoxiong, Wei Qiang, and David P. Weliky. 2007. "Investigation of Finite-Pulse Radiofrequency-Driven Recoupling Methods for Measurement of Intercarbonyl Distances in Polycrystalline and Membrane-Associated HIV Fusion Peptide Samples." *Magnetic Resonance in Chemistry* 45 (S1): S247–60. https://doi.org/10.1002/mrc.2160.

Zhou, Donghua H., Andrew J. Nieuwkoop, Deborah A. Berthold, Gemma Comellas, Lindsay J. Sperling, Ming Tang, Gautam J. Shah, Elliott J. Brea, Luisel R. Lemkau, and Chad M. Rienstra. 2012. "Solid-State NMR Analysis of Membrane Proteins and Protein Aggregates by Proton Detected Spectroscopy." *Journal of Biomolecular NMR* 54 (3): 291–305. https://doi.org/10.1007/s10858-012-9672-z.

Zinke, Maximilian, Pascal Fricke, Sascha Lange, Sophie Zinn-Justin, and Adam Lange. 2018. "Protein−Protein Interfaces Probed by Methyl Labeling and Proton-Detected Solid-State NMR Spectroscopy." *Chemphyschem* 19 (19): 2457–60. https://doi.org/10.1002/cphc.201800542.